

The role of Reynolds number in the fluid-elastic
instability of cylinder arrays

THE ROLE OF REYNOLDS NUMBER IN THE FLUID-ELASTIC
INSTABILITY OF CYLINDER ARRAYS

BY

ALI GHASEMI, B.Sc.

A THESIS

SUBMITTED TO THE SCHOOL OF COMPUTATIONAL SCIENCE AND ENGINEERING

AND THE SCHOOL OF GRADUATE STUDIES

OF MCMASTER UNIVERSITY

IN PARTIAL FULFILMENT OF THE REQUIREMENTS

FOR THE DEGREE OF

MASTER OF SCIENCE

© Copyright by Ali Ghasemi, May 2015

All Rights Reserved

Master of Science (2015)
(School of Computational Science and Engineering)

McMaster University
Hamilton, Ontario, Canada

TITLE: The role of Reynolds number in the fluid-elastic instability of cylinder arrays

AUTHOR: Ali Ghasemi
B.Sc., (Mechanical Engineering)
Sharif University of Technology, Tehran, Iran

SUPERVISOR: Dr. Nicholas Kevlahan

NUMBER OF PAGES: xiii, 60

To my parents, Masoumeh and Mohammad.

Abstract

The onset of fluid-elastic instability in cylinder arrays is usually thought to depend primarily on the mean flow velocity, the Scruton number and the natural frequency of the cylinders. Currently, there is considerable evidence from experimental measurements and computational fluid dynamic (CFD) simulations that the Reynolds number is also an important parameter. However, the available data are not sufficient to understand or quantify this effect. In this study we use a high resolution pseudo-spectral scheme to solve 2-D penalized Navier-Stokes equations in order to accurately model turbulent flow past cylinder array. To uncover the Reynolds number effect we perform simulations that vary Reynolds number independent of flow velocity at a fixed Scruton number, and then analyze the cylinder responses. The computational complexity of our algorithm is a function of Reynolds number. Therefore, we developed a high performance parallel code which allows us to simulate high Reynolds numbers at a reasonable computational cost.

The simulations reveal that increasing Reynolds number has a strong de-stabilizing effect for staggered arrays. On the other hand, for the in-line array case Reynolds number still affects the instability threshold, but the effect is not monotonic with increasing Reynolds number. In addition, our findings suggest that geometry is also an important factor since at low Reynolds numbers critical flow velocity in the staggered

array is considerably higher than the in-line case. This study helps to better predict how the onset of fluid-elastic instability depends on Reynolds number and reduces uncertainties in the experimental data which usually do not consider the effect of Reynolds number.

Acknowledgements

First and foremost, I would like to thank my supervisor, Dr. Nicholas Kevlahan, for his guidance, insight, and patience. He generously offered me his experience and led me into the fascinating field of fluid-structure interaction. In addition, I highly appreciate him dedicating his own parallel machine for this research, without which the numerical study could not be performed easily. I would also like to extend my thanks to Dr. Pawel Pomorski, not only for his technical support, but for his friendly advice and suggestions. Lastly, I wish to express my sincere thanks to my family for their kindness, encouragement and emotional support throughout the study.

Notation and abbreviation

Symbol	Description
f	Frequency
f_N	Natural frequency
f_s	Vortex shedding frequency
\mathbf{u}	Fluid velocity
D	Tube diameter
P	Pitch size (center to center)
B	Tube length
U_g	Gap based mean flow velocity
U_∞	Upstream mean flow velocity
\mathbf{F}	Force
A_y	Transverse flow direction vibration amplitude
ν	Fluid kinematic viscosity
ρ	Fluid Density
m	Mass per unit length
ξ	Damping factor
\mathbf{u}'	Turbulent fluctuating fluid velocity
t	Time

b	Viscus damping coefficient
k	Spring constant
m_A	Added mass
ω	Vorticity
Ω	Physical domain
Ω_i	Penalized (solid) domain
Ω_f	Fluid domain
η	Penalization parameter
∇	Vector differential operator
α	Restitution coefficient
CFL	Courant-Friedrichs-Lewy number
λ	Boundary layer thickness
Re	Reynolds number
Sc	Scruton number
St	Strouhal number
\mathbf{x}	A point in Ω
N	Number of Grid points
N_c	Number of tube rows
N_p	Number of processors
L	Physical domain width

Contents

Abstract	iv
Acknowledgements	vi
Notation and abbreviation	vii
1 Introduction	1
2 Flow-induced Vibration (FIV) in Cylinder Arrays	6
2.1 Vortex-induced vibration (VIV)	7
2.2 Fluid-elastic (self-excited) vibration (FEI)	8
2.3 Turbulence (random) buffeting	11
2.4 Determination of instability in tube arrays	13
3 Numerical Simulation and Modeling	16
3.1 Fluid equations	17
3.2 Cylinder equations	19
3.3 Numerical scheme	21
3.4 Parametrization of the numerical method	24
3.5 Algorithm	27

4	High Performance and Parallel Computation	32
5	Simulation Results and Discussion	39
5.1	Basic parameters of the simulation	40
5.2	Reynolds number and Strouhal number	41
5.3	Effect of Reynolds number on fluid-elastic instability in an in-line square array	44
5.4	Effect of Reynolds number on fluid-elastic instability in a staggered square array	48
5.5	Discussion	51
6	Conclusions and Outlook	54
	Bibliography	60

List of Figures

1.1	The basic cross-sectional patterns for tube layout in heat exchangers: (a) normal-triangular, (b) rotated-triangular, (c) normal or in-line square, and (d) rotated or staggered square [23].	4
2.1	Kármán vortex street, showing flow past a cylinder generating an array of vortices.	7
2.2	Strouhal number as a function of geometry for in-line arrays (Fitzhugh, 1973) [13].	9
2.3	Onset of fluid-elastic instability as a function of Scruton number (Blevins, 1984).	12
2.4	Different types of a cylinder response in an array subjected to cross-flow: (a) vortex-induced vibrations, (b) fluid-elastic (self-excited) vibrations, (c) Turbulence buffeting (random excited), (d) total response caused by all mechanisms (modified from Chen, 1985) [8]. The instability threshold is defined by: (e) the onset of fluid-elastic instability threshold, or (f) maximum allowed vibration amplitude size.	14
3.1	Penalization zone for a single cylinder per periodic domain case.	19
3.2	(a) Discretized domain, (b) vorticity field visualization for in-line array when the flow is statistically stationary.	24

4.1	Domain decomposition for distributed parallel processing	33
4.2	Time step size as a function of time (adaptive time stepping).	35
4.3	(a) Strong scaling for 2048×2048 and 1024×1024 problem sizes, (b) weak scaling for a fixed problem size of 256×256 per processor.	36
4.4	High resolution flow simulation (vorticity field at $Re_g = 60,000$).	38
5.1	Lift force (C_L) frequency spectrum at (a) $Re_\infty = 100$ (b) $Re_\infty = 200$ (c) $Re_\infty = 400$ (d) $Re_\infty = 800$ (e) $Re_\infty = 1600$ [upstream flow velocity based], for fixed in-line and rotated arrays.	43
5.2	Modified plot of Strouhal number versus Reynolds number in rotated square array (Price, Païdoussis and others, 1995) [25]. Black symbols correspond to experimental measurements for different rows in the ar- ray and added red diamond signs denote to the simulation results.	44
5.3	Onset of fluid-elastic instability as a function of Reynolds number and reduced flow velocity in (a) the in-line square array (b) the staggered square array. Based on experimental results, in figure (a) lines 1 and 2 correspond to the mean and lower bound on critical flow velocities, respectively. In figure (b) lines 1 corresponds to the mean critical flow velocities for different geometries and line 2 for the rotated array.	46
5.4	Vorticity fields at (a) $Re_g = 300$, (b) $Re_g = 600$, (c) $Re_g = 1200$, (d) $Re_g = 2400$, (e) $Re_g = 4800$, (f) $Re_g = 9600$, for moving in-line cylinder array subjected to cross flow at $U_g = 9.0$	47

5.5	Cylinder response as a function of pitch-to-diameter (P/D) in the in-line array with fixed gap flow velocity of 9.0 and Reynolds number of $Re_g = 600$. Critical line denotes to the critical point using Blevins experimental data (see figure: 2.3).	49
5.6	Vorticity fields at (a) $Re_g = 210$, (b) $Re_g = 425$, (c) $Re_g = 850$, (d) $Re_g = 1700$, (e) $Re_g = 3400$, (f) $Re_g = 6800$, for moving rotated cylinder array subjected to cross flow at $U_g = 21.2$	50
5.7	(a) Cylinder response at unstable regions for an in-line and a staggered array compared to a sine function with equal RMS values. (b) The corresponding histogram of cylinder positions for the same cylinder arrays, compared to sine function.	53

Chapter 1

Introduction

Cylinder arrays consist of parallel cylinders in a geometrically repeated pattern and are widely found in heat exchangers, boilers, condensers and steam generators in the form of hollow tubes. Hundreds to thousands of tubes are typically used in heat exchangers depending on the application [23]. Cylinder arrays (tube bundles) in these equipments are mostly subjected to cross-flow, interacting with external fluid streams which is hotter or colder than the internal flow within the tubes. In addition, there are other important cases similar to cross flow in cylinder arrays. For instance, when several slender and closely located buildings are exposed to the high speed wind. This problem emerges in the field of wind engineering and is studied carefully in order to predict the effects of wind on the structures.

Analysis of such problems could be classified in the *fluid-structure interaction* (FSI) problems since, depending on the design, tubes often move or bend due to the external fluid forces. Consequently, the fluid flow is also modified by the motion of the tubes. This is therefore a strongly nonlinear coupled problem. Figure (1.1) depicts various configurations of the circular tube arrays for different industrial applications

[8]; however in this study, we focus on two cases: in-line and rotated square arrays. Table (1.1) also presents the important non-dimensional parameters that are useful to characterize and analyze this problem.

Flow-induced periodic movements (oscillations) of the tubes may cause sudden destruction, especially in tightly packed arrays, if the vibration amplitude exceeds a critical threshold. This phenomenon was not properly identified until 1960s and led to many project failures. MacDonald et al (1996) reported a large list of tube failures specifically in steam generators in power generator plants [19]. The cost of damages in power generation industry due to the failure of designs is estimated approximately \$1000 M over a decade [23]. Therefore, it urgent to improve the design standards for such equipment in order to avoid damage. Damage caused by flow-induced vibration is not limited to equipment containing tube arrays. In 1965 three of eight cooling towers arranged in two parallel staggered rows at the Ferrybridge power station in England collapsed suddenly [27] [at an estimated cost of \$700,000 to \$840,000 each]. The failure of those newly built towers was attributed to the synchronization of the wind-induced vibrations with the natural frequency of the structure. These incidents and some other similar project failures accentuated the importance of flow-induced vibration in arrays of cylindrical structures.

Many attempts have been performed by researchers and engineers to study better this particular FSI problem over the past decades. Y.N. Chen (1970) presented a map of Strouhal numbers for cylinder arrays as a function of geometry and gap spacing [11] and the data have been widely used for industrial designs by engineers. Connors (1969) introduced self-excitation phenomenon in tube arrays caused by energy transfer from fluid flow to cylinders. He proposed a simplified theory, the displacement

mechanism, to evaluate tubes instability which was named *fluid-elastic instability* after a few years [12]. Later on, other researchers also developed investigation of the fluid-elastic instability. Weaver and co-workers (1982) developed a theoretical model for fluid-elastic instability in which instability was attributed to the movement of the separation point on the tube surfaces [18]. Price and Paidoussis (1984) proposed a quasi-static model for the flow-induced forces to analyze the instability for the case of one-degree-of-freedom mechanism [24]. Chen (1987) introduced a new model in which fluid forces were simply defined by a function of the tube position, velocity, and acceleration [9]. The function needs some experimental measurements to be evaluated; otherwise, the method is not considered useful. Blevins (1984) based on some experimental data proposed a guideline for heat-exchanger design. He introduced critical flow velocity as a function of mass-damping ratio of tubes and accounted less on other parameters such as geometry or gap spacing [4],[5]. None of these experimental/theoretical models of fluid-elastic instability accounted sufficiently to the role of turbulence intensity or Reynolds number. Many other theoretical, experimental and numerical investigations have been performed by other researchers and now cylinder excitations are attributed to four different mechanisms, namely: *vortex-induced vibrations (VIV)*, *turbulence buffeting*, *acoustic excitation* and *fluid-elastic instability (FEI)*. In this study, our main focus is the FEI mechanism which is considered the most dangerous phenomenon that can happen in heat exchangers.

Analysis of the cross-flow in cylinder array using analytical or numerical/computational approaches is complicated for two main reasons. First, the geometry of the structure changes due to the excitations caused by acting fluid forces. Secondly, the flow has a complex coherent vortex shedding structure and also becomes turbulent due to the

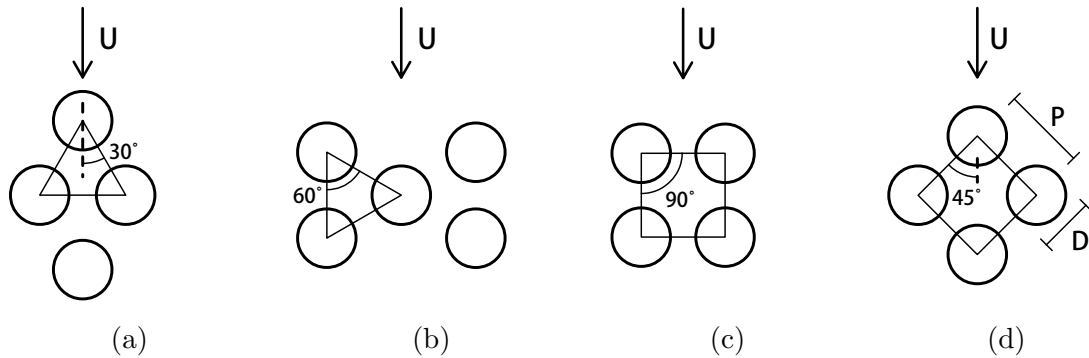


Figure 1.1: The basic cross-sectional patterns for tube layout in heat exchangers: (a) normal-triangular, (b) rotated-triangular, (c) normal or in-line square, and (d) rotated or staggered square [23].

high level of interaction of fluid with cylinders.

As the thesis title indicates, the effect of Reynolds number on instability of tube arrays is our main concern in this study. The available data on the effect of turbulence intensity and Reynolds number is conflicting. Knowing that turbulent level depends on Reynolds number, Franklin and Soper (1977) claimed that turbulence *decreases* fluid-elastic instability threshold [14], while experimental data of Southworth and Zdravkovich (1975) suggest that turbulence has *stabilizing* effect for the in-line case [29]. In order to untangle this problem, we take advantage of simulations to perform numerical experiments which are very difficult to perform physically in laboratories. The reason is that for a fixed flow velocity, Reynolds number is a function of fluid kinematic viscosity and this makes it difficult to qualify the effect of Reynolds number and cross-flow velocity separately. In reality, changing viscosity is not easy, since it is one of fluid properties and is a function of quality (vapor mass ratio), pressure and/or temperature. The best attempt to study this problem experimentally was performed

Table 1.1: Key non-dimensional parameters for a cylinder array subjected to cross-flow [5],[22].

Non-dimensional parameter	Definition	Physical meaning
Reduced velocity (U_r)	$\frac{U}{f_N D}$	normalized flow velocity
Dimensionless amplitude	$\frac{A_y}{D}$	vibration amplitude / tube width
Reynolds number (Re)	$\frac{UD}{\nu}$	inertia force / viscus force
Strouhal number (St)	$\frac{f_s D}{U}$	normalized vortex shedding frequency
Scruton number (Sc)	$\frac{m\xi}{\rho D^2}$	Mass ratio \times damping factor
Turbulence intensity (TI)	$\frac{\langle u' \rangle}{U}$	RMS of turbulence / mean flow velocity

by Mewes & Stockmeier (1991) [21], who made measurements on flow induced instabilities in cylinders using a fluid with different viscosities ($0.7 \leq \nu/\nu_{water} \leq 87.3$); this was achieved by mixtures of water and organic substances. They were successful in stabilizing cylinders by varying ν/ν_{water} from 2.52 to 0.7. This was real and unique evidence that the Reynolds number is an important parameter which needs to be accounted for properly in the theoretical models and is our motivates our numerical study.

In the following, we will first describe physics of the problem and the flow-induced vibration phenomenon in sufficient details (chapter 2), and then we will present the mathematical model (2-D incompressible Navier-Stokes), the numerical method (pseudo-spectral scheme), the algorithm and the computational tool that we used to attack this problem (chapter 3, 4). We will finally demonstrate the simulation outcomes, discussing the results (chapter 5) and summarizing the main conclusions of the study at the end (chapter 6).

Chapter 2

Flow-induced Vibration (FIV) in Cylinder Arrays

Flexibly mounted cylinder arrays, subjected to cross flow, begin to vibrate due to the energy gained from the fluctuating forces (drag and lift), exerted by fluid. A fluid flow passed a fixed cylinder array has a complicated structure; however, interaction of the moving cylinders with the fluid and adjacent cylinders increases the flow complexity to a greater extent. Understanding this phenomenon is of primary importance and later in chapter 5 we will analyze the thresholds of instabilities in tube arrays, by focusing on different mechanisms and parameters.

In this chapter we aim to review various types of vibrational responses and instabilities of cylinders in cross-flow, caused by different mechanisms such as lock-in, fluid-elastic instability and turbulence buffeting (excluding acoustic excitation), using the classification introduced by S.S. Chen (figure: 2.4). In particular, we consider the effects of parameters such as flow velocity, turbulence level, Scruton number, natural frequency and geometry of the array on the instabilities.



Figure 2.1: Kármán vortex street, showing flow past a cylinder generating an array of vortices.

2.1 Vortex-induced vibration (VIV)

When a fluid passes a structure, it generates vortices periodically in the wake region behind the body. This phenomenon (also known as Kármán vortex shedding) imposes a periodic surface pressure on the body, due to its periodicity, causing flexible structures to oscillate. The vortex street formed behind the structure and parallel to the flow direction, regardless of the geometry of the structure, are usually similar (figure: 2.1) [5]. The vortex shedding frequency, is characterized by a non-dimensional parameter, called Strouhal number and defined as

$$St = \frac{f_s D}{U}, \quad (2.1)$$

where f_s is the vortex shedding frequency, U the flow velocity (based on mean or upstream flow velocity), and D is the characteristic length (hydraulic diameter¹) of the structure. Figure (2.2) suggests experimental values of Strouhal number for in-line square cylinder arrays for different configurations [13].

Strouhal number is very important because cylinders become excited if the vortex shedding synchronizes with the cylinder oscillation at a frequency close to one of the natural mechanical frequencies of the cylinder (2.4a). Since the rate of input energy

¹ $D_H = \frac{4A}{P}$, which A is the cross-section area and P is the cross-section perimeter of the body.

exceeds the rate of energy damped in the array, high amplitude vibrations (resonance) occurs. This phenomenon is known as *lock-in* mechanism and in tube arrays must be avoided due to the possibility of destroying the tube bundle. ASME designing standards [3] suggest an empirical equation for the range of frequency ratios to be avoided for lock-in in cylinder arrays (2.2):

$$|f_s - f_N| \leq 0.3f_N \text{ (or } 0.2f_N\text{)}. \quad (2.2)$$

At the end of this part, we highlight some important facts. First, for unsteady flows synchronization might not be easily avoided since the vortex shedding frequency might vary and get close to the natural frequency. Secondly, it is the lock-in phenomenon that initiates temporary oscillations in the cylinders in which higher amplitude vibrations (or instability) might happen consequently, due to other excitation mechanisms [7]. Thirdly, synchronization mostly occurs in transverse oscillations (caused by lift force); however, high-density fluid flows can induce stream-wise vibrations at a frequency, approximately twice the vortex shedding frequency ($2f_s$) [7, 22].

2.2 Fluid-elastic (self-excited) vibration (FEI)

Roberts in 1966, was probably the first to observe that a single row of tubes responded to cross-flow by high amplitude transverse vibrations, well outside the lock-in region. He proposed that the time lag between fluid forces and cylinders displacement (response) is the cause of such behavior [26]. Four years later, Connors suggested a displacement-induced vibration mechanism as the main cause of this phenomenon, by considering the induced flow forces variation due to the interaction of adjacent

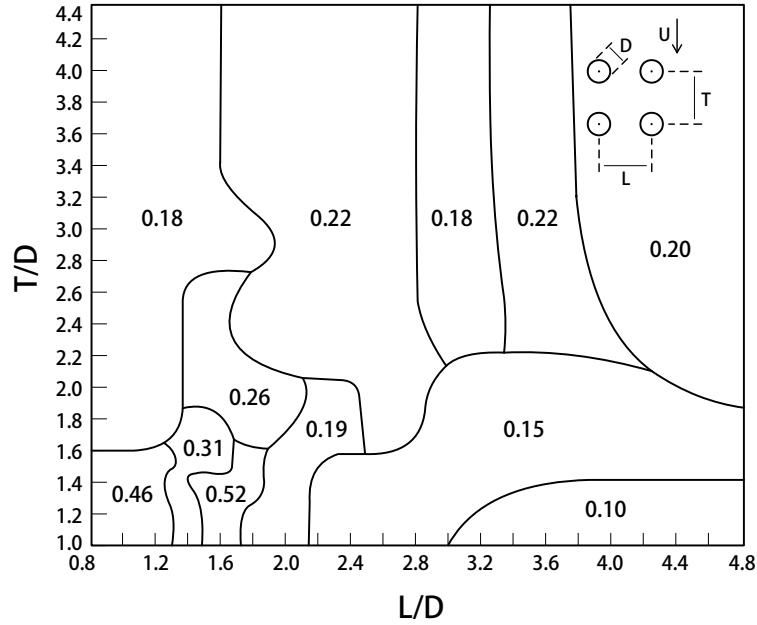


Figure 2.2: Strouhal number as a function of geometry for in-line arrays (Fitzhugh, 1973) [13].

cylinders [12]. Later, this phenomenon was named “*fluid-elastic instability*”.

Fluid-elastic instability occurs suddenly both in cylinder rows and in cylinder arrays when the flow velocity exceeds a critical value (figure: 2.4b), causing vibrations with amplitude proportional to U^5 [5]. This type of instability has been reported to be the main cause of short term damage in heat exchangers [23].

Based on non-dimensional analysis, the onset of the fluid-elastic instability is characterized by the critical flow velocity and may be written as:

$$\frac{U_{cr}}{f_N D} = C \left(\frac{m}{\rho D^2} \right)^a (2\pi\xi)^b \left(\frac{P}{D} \right)^c \left(\frac{UD}{\nu} \right)^d \left(\frac{u'}{U} \right)^e \dots \quad (2.3)$$

where:

U_{cr}	=	The critical mean velocity across gap between tubes
f_N	=	Natural frequency of tubes
D	=	Tube diameter
P	=	Pitch size (center-to-center)
m	=	Mass per unit length plus added mass
ξ	=	Damping factor
ρ	=	Fluid density
ν	=	Kinematic viscosity.

and a , b , c , d , e and C are empirically determined parameters. Many experiments as well as theories have been performed/developed to attempt to predict fluid-elastic instabilities. Here, two criteria for the fluid-elastic instability will be represented. Chen, in 1985, established a conservative approach for critical velocity based on all the experimental and theoretical measurements available at that time. In this approach, the critical velocity depends on parameters such as mass ratio, damping factor and natural frequency of the cylinders as well as geometry of the array [5]. Assuming this, the equation (2.3) could be rewritten as:

$$\frac{U_{cr}}{f_n D} = a \delta_s^b \quad \text{where} \quad \delta_s = \frac{m_V \xi_V}{\rho D^2}, \quad (2.4)$$

in which, constants a , b are given in table (2.1) and subscript V means the values are measured in vacuum, and the given U_{cr} would be a conservative value for the onset of instability [8].

Another useful and widely referred experimental data for prediction of the fluid-elastic instability is the empirical data published by Blevins in 1984 [4], which simply shows the stable and unstable region based on Scruton number and geometry of the array (figure: 2.3). We will mostly refer to these data, since both the lower bound

(conservative) and the mean value of the critical velocity are illustrated.

Both criteria presented above have been confirmed by later investigations. However, there are some important facts to be pointed out. First, the values for critical velocities are based on statistical experimental results. This means when referring to these data, we should be careful whether they are lower bound (conservative) or mean values of critical velocity. Implementing uncertainty quantification methods might be helpful, due to the chaotic nature of the cross-flow and existence of random behavior. Secondly, parameters such as cylinder natural frequency or damping factor are (mostly) defined in vacuum. In this manner, slightly different values of critical velocity respect to actual values are expected, since the cylinder motions are coupled with the adjacent fluid. And finally, there is no clear information about the range of Reynolds number that those data are valid. In other words, although the dependency of the critical velocity on parameters such as geometry or Scruton number has been measured in previous investigations, the available data gives conflicting evidence about the relation between the Reynolds number or turbulence intensity on the fluid elastic instability [5].

2.3 Turbulence (random) buffeting

In turbulent flow random pressure distributions on surface of cylinders induce low amplitude vibrations in which the excitation level depends on turbulence intensity (TI) and the random behavior of the flow, due to the upstream flow turbulence or the turbulence generated in the tube array. In general turbulence level increases with increasing Reynolds number and turbulence intensity level [8]. Figure (2.4c) shows

Table 2.1: Lower bounds on critical velocity in tube arrays [8].

Tube array	a	b	Range for δ_s
Tube row	$1.35(T/D - 0.375)$	0.06	$0.05 < \delta_s < 0.3$
	$2.30(T/D - 0.375)$	0.50	$0.30 < \delta_s < 4.0$
	$6.00(T/D - 0.375)$	0.50	$4.0 < \delta_s < 300$
Square array	2.1	0.15	$0.03 < \delta_s < 0.7$
	2.35	0.5	$0.7 < \delta_s < 300$
Rotated square array	$3.54(T/D - 0.5)$	0.5	$0.1 < \delta_s < 300$
Triangular array	$3.58(T/D - 0.9)$	0.1	$0.1 < \delta_s < 2$
	$6.53(T/D - 0.9)$	0.5	$2 < \delta_s < 300$
Rotated triangular array	2.8	0.17	$0.01 < \delta_s < 1$
	2.8	0.5	$1 < \delta_s < 300$

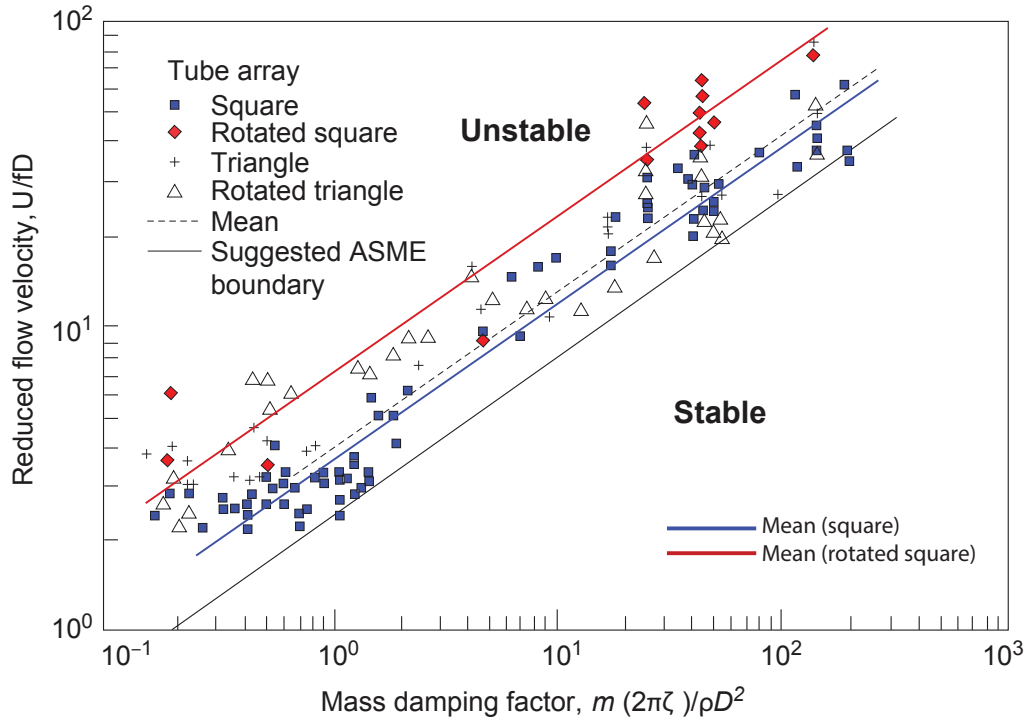


Figure 2.3: Onset of fluid-elastic instability as a function of Scruton number (Blevins, 1984).

how the vibration amplitude varies with flow velocity (and also Reynolds number). The turbulence induced vibration amplitude is not usually high enough initially to cause instability. However, random excitation induce or modify lock-in or fluid-elastic instability. Some experiments have demonstrated that the upstream turbulence intensity can stabilize or destabilize self-excited vibrations by increasing or decreasing the critical velocity. On the other hand, other experiments have shown little or no effect of turbulence on instabilities. In 1981, Chen and Zembrzejczyk [10] performed water-tunnel tests that partially resolved this problem; depending on the turbulence characteristics of the flow, both stabilizing and destabilizing effects exists. Although this statement was verified later by Soper in 1981 [28], this question still remains that how turbulence can affect the instabilities in tube arrays.

2.4 Determination of instability in tube arrays

In the previous sections, different flow-induced vibration mechanisms, namely: vortex-induced, turbulence buffeting and fluid-elastic vibration were described. These flow-induced vibrations may cause instability in tube arrays, leading to damages. The an important question regarding flow-induced vibration is how instability could be defined.

Generally there are different ways to define instability in cylinder arrays; however, we introduce two of the most widely used definitions. The first definition which corresponds exclusively to the onset of fluid-elastic instability, specifies the critical condition in a way that a cylinder oscillation amplitude increases suddenly with a relatively sharp slope if the flow velocity exceeds a certain value. This critical threshold

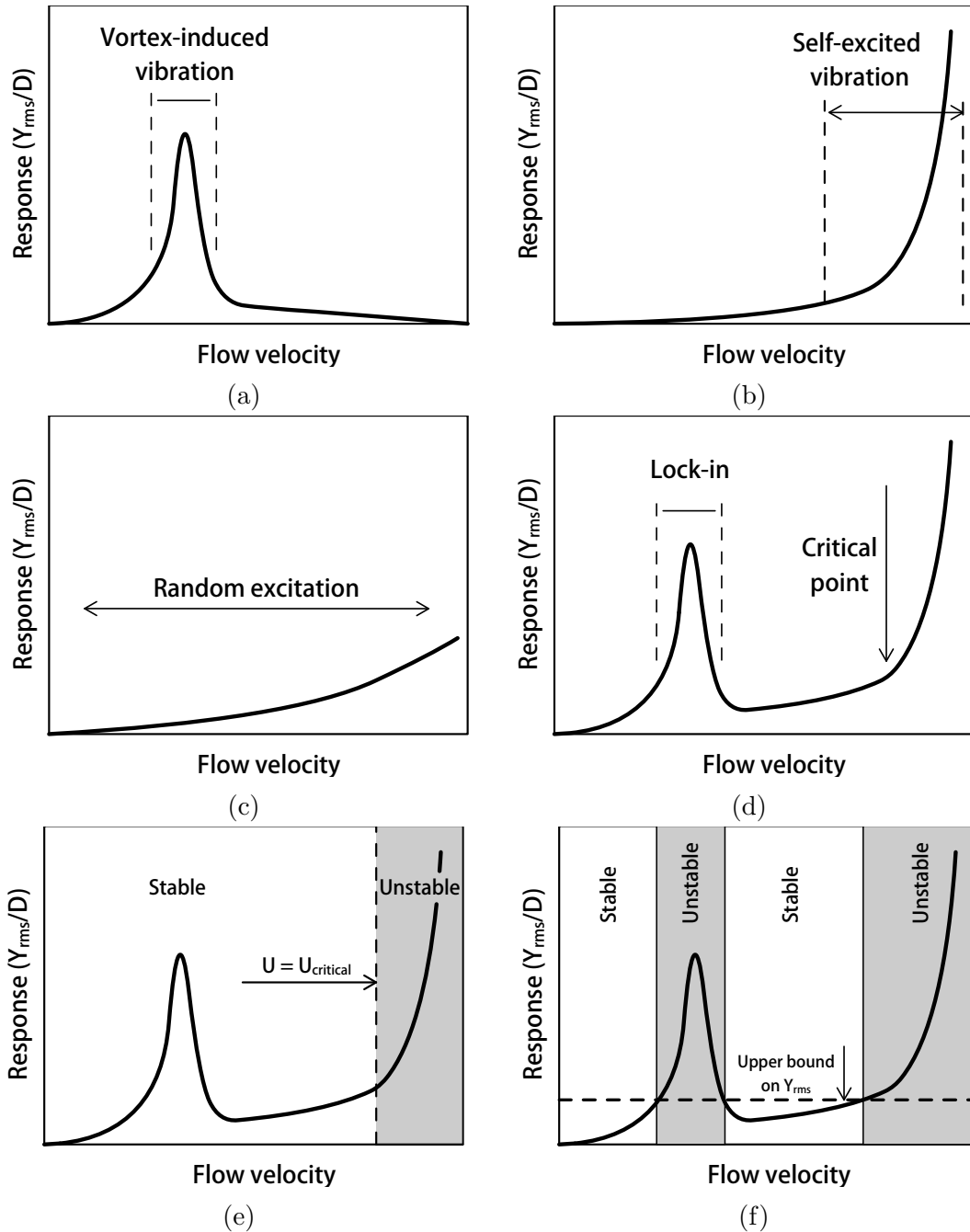


Figure 2.4: Different types of a cylinder response in an array subjected to cross-flow: (a) vortex-induced vibrations, (b) fluid-elastic (self-excited) vibrations, (c) Turbulence buffeting (random excited), (d) total response caused by all mechanisms (modified from Chen, 1985) [8]. The instability threshold is defined by: (e) the onset of fluid-elastic instability threshold, or (f) maximum allowed vibration amplitude size.

is called critical point (figure: 2.4e). In this approach, for a certain array, assuming that Y_{rms} is proportional to U^n , critical velocity is defined as the point that n suddenly changes from ~ 1 to a value of ~ 5 .

Another definition for instability, which is based on industrial standards, is when oscillation amplitudes (RMS or maximum values) exceed a certain value. This approach, unlike the previous method, considers both resonant and non-resonant instabilities (figure: 2.4f); however, it might not always give the same critical point for fluid-elastic instability as defined by first approach. In the following chapters we will refer to the second definition in order to define the onset of fluid-elastic instability, since it is an appropriate and universal approach.

Chapter 3

Numerical Simulation and Modeling

In the previous chapters we mainly focused on the physical aspects of moving tube arrays subjected to cross-flow. In this chapter we describe the procedure that we use to efficiently and accurately model the problem in order to better analyze the role of Reynolds number in the onset of fluid-elastic instability. We start this chapter with a mathematical formulation for modeling fluid flow past cylinder arrays, and then the numerical methods used for solving those mathematical models are described. After that, dynamical modeling of cylinders interacting with fluid or other cylinders are discussed. Since computational cost and efficiency of the method is of primary importance, some noticeable features of the numerical method that determines the efficiency of the simulation are analyzed in detail. At the end of the chapter our algorithm (pseudo-code) for computing the our numerical methods is described.

3.1 Fluid equations

In this section we describe concisely the theoretical model used for this particular fluid-structure interaction problem, developed by Kevlahan and Ghidaglia [16]. Before going further, it should be pointed out that we are considering a 2-D flow by assuming negligible 3-D effects based on previous investigations performed by Kevlahan [17]. This assumption is reasonable because the problem is geometrically uniform in the span-wise direction in which span-wise vortices are dominant compared to stream-wise and transverse flow direction vortices. In addition, the cylinder motions tend to synchronize vortex shedding in the span-wise direction and higher vibration amplitudes increase the span-wise correlation. This case is different than homogeneous isotropic turbulence and the vortex shedding mechanism is similar to Kármán vortex street. Therefore, for this particular fluid-structure interaction problem a 2-D flow assumption is accurate and consistent with the flow structure. In general, for a viscous fluid flow we can write Navier-Stokes equations as

$$\frac{\partial \mathbf{u}}{\partial t} + (\mathbf{u} + \mathbf{U}_\infty) \cdot \nabla \mathbf{u} + \frac{1}{\rho} \nabla P = \nu \Delta \mathbf{u}, \quad (3.1)$$

in which \mathbf{u} and \mathbf{U}_∞ denote to the local and upstream fluid velocity, respectively. P is the absolute pressure, ρ the fluid density and ν the viscosity. And the mass continuity equation (conservation of mass) for incompressible flow could be expressed as

$$\nabla \cdot \mathbf{u} = 0. \quad (3.2)$$

Equations 3.1 and 3.2 only model fluid flow. Therefore, in order to define a solid zone in the problem domain for cylinders with practically no permeability and

satisfying no-slip condition on the solid-fluid contact surface, we use the Brinkman volume penalization method by adding a new term to the Navier-Stokes equation. Now, instead of \mathbf{u} in the equations (3.1,3.2), we are solving for \mathbf{u}_η as

$$\frac{\partial \mathbf{u}_\eta}{\partial t} + (\mathbf{u}_\eta + \mathbf{U}_\infty) \cdot \nabla \mathbf{u}_\eta + \frac{1}{\rho} \nabla P = \nu \Delta \mathbf{u}_\eta - \frac{1}{\eta} \chi(\mathbf{x}, t) (\mathbf{u}_\eta + \mathbf{U}_\infty - \mathbf{U}_{o,i}), \quad (3.3)$$

and

$$\nabla \cdot \mathbf{u}_\eta = 0, \quad (3.4)$$

whereas $\mathbf{U}_{o,i}$ is the i^{th} cylinder velocity and η is the penalization parameter (permeability constant) which is very small ($0 < \eta \ll 1$). The characteristic function $\chi(\mathbf{x}, t)$ defines the solid regions to be penalized, and is defined as

$$\chi(\mathbf{x}, t) = \begin{cases} 1 & \text{if } \mathbf{x} \in \Omega_i \quad \forall i, \\ 0 & \text{otherwise,} \end{cases} \quad (3.5)$$

in which Ω_i denotes i^{th} solid zone (cylinder) as shown in the figure (3.1). It has been proved by Carbou and Fabrie (2003) that the solution of equations (3.3, 3.4) converges to the solution of incompressible Navier-Stokes (3.1, 3.2) and the upper bound on global error of the penalized Navier-Stokes is [6]

$$\|\mathbf{u} - \mathbf{u}_\eta\|_2 \leq C\eta^{\frac{1}{2}}, \text{ in } L^2(\Omega_f). \quad (3.6)$$

By the Brinkman volume penalization method, the no-slip condition will be imposed automatically since the solution for \mathbf{u}_η always equals to the cylinder velocity ($\mathbf{U}_{o,i}$) on the edge of fluid-solid surface. A doubly periodic 2-D domain for the problem has

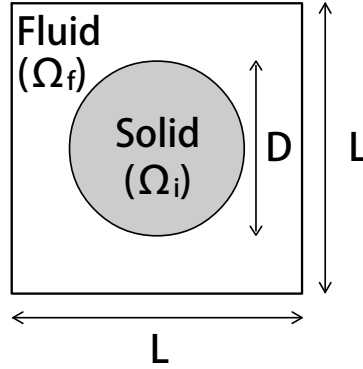


Figure 3.1: Penalization zone for a single cylinder per periodic domain case.

been assumed which is quite consistent with the physics of the problem, an array of periodic tubes with repeated pattern. The boundary conditions on equations (3.3,3.4) are summarized below:

$$\begin{cases} \mathbf{u} + \mathbf{U}_\infty = \mathbf{U}_{o,i} & \text{on } \Omega_i \quad \forall i, \\ \mathbf{u} \text{ is } Q\text{-periodic, } & Q =]0, L[\times]0, L[. \end{cases} \quad (3.7)$$

3.2 Cylinder equations

So far we have described how fluid flow has been modeled in a periodic domain, with presence of fixed solid zones (penalized regions). As we discussed in chapter 2, our goal is to analyze the vibration of cylinders induced by fluid forces. In this section, our focus is mechanical response of the cylinders. The fluid forces acting on the surface of cylinders (\mathbf{F}_i) are calculated by integrating the penalization term over the cylinders simply as [1]

$$\mathbf{F}_i = \frac{1}{\eta} \oint_{\Omega_i} (\mathbf{u} + \mathbf{U}_\infty - \mathbf{U}_{o,i}) d\mathbf{x}. \quad (3.8)$$

It has been proved analytically that the error of calculated forces are only $O(\eta^{\frac{1}{2}})$ [2] and it was shown by Kevlahan (2005) [17] that the error for computed drag force is about 1% if $\eta = 10^{-4}$ (for non-dimensional variables). Considering fluid forces to be the only external forces acting on the cylinders, the motion of cylinders is modeled by the damped harmonic oscillation equation as

$$(m + m_A) \frac{\partial^2 \mathbf{X}_{o,i}}{\partial t^2} + b \frac{\partial \mathbf{X}_{o,i}}{\partial t} + k \mathbf{X}_{o,i} = \mathbf{F}_i, \quad (3.9)$$

where $\mathbf{X}_{o,i}$ are cylinder positions, m is mass per unit length of cylinders, m_A the added mass¹, b damping factor and k the spring constant². Fluid forces acting on i^{th} cylinder is computed using equation (3.8). The added mass for fixed cylinder arrays are calculated by [5]

$$m_A = \frac{\rho_f \pi D^2 B}{4} \left[\frac{(D_e/D)^2 + 1}{(D_e/D)^2 - 1} \right], \text{ where } D_e/D = \left(1 + \frac{1}{2}(P/D) \right) P/D, \quad (3.10)$$

in which B is the length of cylinders. Using equation (3.8), we compute forces to plug into equation (3.9) which is a simple ODE problem.

At the end of this section we consider a case in which two or more cylinders can clash or hit each other. This phenomenon mostly happens in tightly packed arrays and when cylinders are highly unstable or they have anti-phase vibrations. Although we can easily observe the collision between cylinders during the simulation, interpret it as an unstable case and stop the simulation, we have seen stable situations in which some initial and transient oscillations caused collisions. So it is necessary to

¹We use a fixed value for added mass, by assuming fixed cylinder array which is consistent with experimental practices.

² k , b are values based on vacuum or uncoupled fluid-cylinder measurements. This assumption is consistent with previous experimental results.

consider the situation when cylinders can collide. Ignoring change of total momentum at the moment of collision³, we can write conservation of momentum for two arbitrary cylinders (i, j) as

$$\begin{cases} \mathbf{U}_{n,i}^k = \frac{1}{2}(1 - \alpha)\mathbf{U}_{n,i}^{k-1} + \frac{1}{2}(1 + \alpha)\mathbf{U}_{n,j}^{k-1}, \\ \mathbf{U}_{n,j}^k = \frac{1}{2}(1 - \alpha)\mathbf{U}_{n,j}^{k-1} + \frac{1}{2}(1 + \alpha)\mathbf{U}_{n,i}^{k-1}, \end{cases} \quad (3.11)$$

and

$$\begin{cases} \mathbf{U}_{t,i}^k = \mathbf{U}_{t,i}^{k-1}, \\ \mathbf{U}_{t,j}^k = \mathbf{U}_{t,j}^{k-1}, \end{cases} \quad (3.12)$$

where $k - 1$, k denote to time steps before and after collision, respectively. α is the restitution coefficient and equals zero for totally elastic and one for completely inelastic impacts. For two steel bodies colliding with small relative velocities, α would be close to one [20]. Notation “n” stands for velocity components in direction of the impact and “t” for direction tangent to contact line between cylinders. It should be remarked that the cylinders might impact in any direction since the domain is periodic.

3.3 Numerical scheme

To solve equations discussed in the previous sections numerically, our strategy is to first calculate the right hand side of equation (3.3) by computing space derivatives and penalization term, and then finding the solution of (\mathbf{u}_η) by integrating the left hand side in time. In order to compute space derivatives, we approximate the solution

³We assume that $\int_t^{t+\delta t} \mathbf{F}_i dt = 0$.

by transforming (\mathbf{u}_η) to Fourier space. To avoid convolution in the advection term of Navier-Stokes, right hand side is calculated partially in real space and partially in Fourier space using discrete Fourier transforms (DFT). This method is known as pseudo-spectral method [31] and the procedure is described in the main computing algorithm (A.1). The solution approximation may be written as Fourier-Galerkin series

$$\mathbf{u}_\eta(x, y, t) = \sum_{k \in Z^2} \mathbf{u}_k(t) \exp[2\pi i (\frac{k_1 x}{L_1} + \frac{k_2 y}{L_2})]. \quad (3.13)$$

It is notable that the solution of equation (3.3) does not necessarily satisfy divergence free condition in equation (3.4). Therefore, a special treatment is needed when computing the right hand side of equation (3.3) before time integration. To satisfy equation (3.4), we project the trend of the solution ($\frac{\partial \mathbf{u}_\eta}{\partial t}$) on the divergence-free plane in Fourier space before final inverse Fourier transform, using

$$\widehat{\frac{\partial \mathbf{u}_\eta}{\partial t}} \Big|_{\text{divergence free}} = \mathbf{P} \widehat{\frac{\partial \mathbf{u}_\eta}{\partial t}}, \quad (3.14)$$

and

$$\mathbf{P} = 1/(K_1^2 + K_2^2) \begin{bmatrix} K_2^2 & -K_1 K_2 \\ -K_1 K_2 & K_1^2 \end{bmatrix}$$

where K_1 , K_2 are wave numbers in two dimensions. We also need to keep the mean value of \mathbf{u}_η fixed to zero during the simulation and eliminate energy lost of the flow. To do this, we simply assign zero to $\widehat{\frac{\partial \mathbf{u}_\eta}{\partial t}}$ if $K_1 = K_2 = 0$. Now, the solution at time $t > t_0$ can be calculated by integrating the computed trend (right hand side of

equation 3.3). We use an explicit, strongly stable, four stage and third order Runge-Kutta method to do this. This member of Runge-Kutta family is described below [30]

$$\begin{cases} \mathbf{U}_1 &= \mathbf{u}_k + \frac{1}{2} \times dt \times \text{TREND}(\mathbf{u}_k) \\ \mathbf{U}_2 &= \mathbf{U}_1 + \frac{1}{2} \times dt \times \text{TREND}(\mathbf{U}_1) \\ \mathbf{U}_3 &= \frac{2}{3}\mathbf{U}_0 + \frac{1}{3}\mathbf{U}_2 + \frac{1}{6} \times dt \times \text{TREND}(\mathbf{U}_2) \\ \mathbf{u}_{k+1} &= \mathbf{U}_3 + \frac{1}{2} \times dt \times \text{TREND}(\mathbf{U}_3). \end{cases} \quad (3.15)$$

We used the same Runge-Kutta method (3.15) to integrate the ODE equation of (3.9) in time. Figure (3.2a) illustrates the discretized domain and penalized zones for case of four cylinders per cell, and figure (3.2b) shows the solution in the form of vorticity (ω) for arbitrary parameters at a time in which the flow is developed.

Finally, it should be mentioned that differentiation using pseudo-spectral method has a high (spectral) accuracy, compared to finite difference or finite volume methods, since it uses all the data in the domain to calculate the derivative at each point. And as equation (3.13) suggests, the solution has been approximated by sines and cosines which means the solution is periodic. So besides its accuracy, we prefer this method because it is consistent with our periodicity assumption for the boundary conditions (3.7) and also with the physics of the problem.

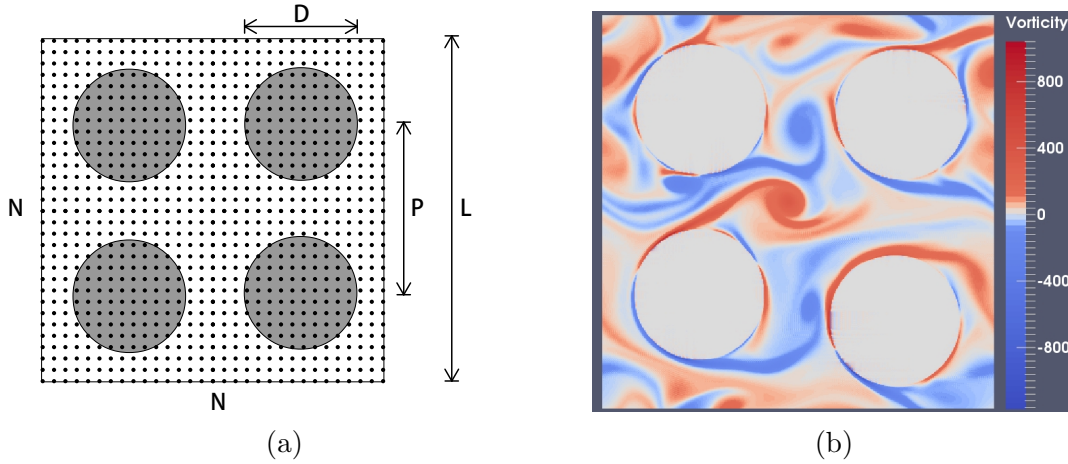


Figure 3.2: (a) Discretized domain, (b) vorticity field visualization for in-line array when the flow is statistically stationary.

3.4 Parametrization of the numerical method

In this part, we focus on some important aspects of our numerical tool such as time and space discretization in more detail. The approach taken here is of primary importance since it helps us to estimate the problem size and computational cost of the method.

Time Discretization: To integrate trend of the solution in time using Runge-Kutta method (3.15), we need to define an appropriate time step size (dt). Time stepping must meet the stability criteria of the method and also give satisfactory accuracy. For our numerical method, the lower bound on time step size based on stability criterion is

$$\Delta t_{stable} \leq \min\left(CFL_1 \cdot \frac{\Delta x}{\max(|\mathbf{u}|)}, CFL_2 \cdot \frac{\Delta x^2}{\nu}\right), \quad (3.16)$$

where for this particular Runge-Kutta scheme, stability conditions are $CFL_1 \leq 2$

and generally $CFL_2 \leq 0.5$. Since stability does not necessarily guarantee the desired accuracy, we need to control the accuracy by a parameter (C) as

$$\Delta t_{accurate} = C\Delta t_{stable}, \quad (3.17)$$

in which we found that $C = 0.5$ gives a satisfactory error of less than $\sim 2\%$ for RMS values of transverse direction oscillations.

An important issue about the time discretization in equation (3.16) is that for high Reynolds numbers kinematic viscosity (ν) is very small and mostly time step size is limited by the first argument of equation (3.16). We also know that $max(|\mathbf{u}|)$ is a function of time. Consequently, the upper bound on time step size is time dependent and this suggests using adaptive time stepping. Adaptation of time step size seems essential since we can keep the stability/accuracy criteria in time; otherwise, conservatively a small time step size must be used. On the other hand, we can take the advantage of adaptation by having temporary higher time step sizes and increase our numerical method efficiency.

Space Discretization: Boundary layer thickness formed around the solid-body (λ) is

$$\lambda \sim \frac{D}{\sqrt{Re}}, \quad (3.18)$$

Based on grid consistency tests [16], at least four grid points are needed to capture the boundary layer. This gives

$$\lambda \geq 4\Delta x = \frac{4L}{N}.$$

Therefore the minimum grid points in each direction of the domain (equi-spaced

points) is

$$N \geq 4N_c \frac{P}{D} \sqrt{Re} \quad (3.19)$$

where N_c is number of cylinder rows (or columns) per computational domain. It should be highlighted that the minimum grid size is a function of Reynolds number for a certain array. This means the higher Re number, the more grid points is needed for numerical simulations. Here, we should point out the fact that grid points are fixed in time. This is the advantage of Brinkman volume penalization method; the solid zones are defined by the equations (3.3, 3.5) and there is no need to move grid points when cylinders move.

Boundary Smoothing: Approximation of a discontinuous function using Fourier series gives some errors like a wavy noise near discontinuity region. This phenomenon is called *Gibbs oscillations* and in order to reduce these errors around the penalized region we need to modify the discontinuous region (equation: 3.5) by smoothing the edge of solid-fluid surface. The formula below shows how the modification is performed:

$$\chi(\mathbf{x}, t) = \frac{1}{2} \left(1 - \tanh\left(\frac{r(x, t) - D/2}{W}\right) \right), \quad (3.20)$$

where r corresponds to the distance from center of cylinder and W is the parameter to control the sharpness of the smoothed band around a cylinder⁴. The solid-fluid boundary is usually smoothed over 3 to 4 grid points.

Mean and Gap velocity: There are two different definitions for the average flow velocity in cylinder arrays. First is the mean upstream flow velocity referred as U_∞ . The second and most commonly used definition is the mean flow velocity in the minimum gap between cylinders, expressed as U_g . For in-line square cylinder arrays,

⁴ χ at $(R - W) - \chi$ at $(R + W) = 0.7616$

the relation between these two definitions is

$$U_g = \frac{P}{P-D} U_\infty. \quad (3.21)$$

For square staggered (rotated) cylinder arrays depending on pitch-to-diameter size, gap flow velocity is

$$\begin{cases} U_g = \frac{\sqrt{2}P}{2(P-D)} U_\infty, & \text{if } 1 < \frac{P}{D} \leq \frac{1}{2-\sqrt{2}}, \\ U_g = \frac{\sqrt{2}P}{\sqrt{2}P-D} U_\infty, & \text{if } \frac{P}{D} > \frac{1}{2-\sqrt{2}}. \end{cases} \quad (3.22)$$

Consequently there are two different Reynolds numbers corresponding to two different definitions of characteristic flow velocities. The Reynolds number based on gap velocity is higher; for example $Re_g = 3Re_\infty$, if $P/D = 1.5$ for in-line square array. In the next chapters we will mostly use the second definition, although previous experimental results are expressed based on both definitions.

3.5 Algorithm

In this section our algorithm for computing the formulas and numerical methods, described in the previous sections is presented. The main code is written based on algorithm (A.1) and using two functions TREND1 (A.2) and TREND2 (A.3).

Function TREND1 (A.2) describes the pseudo-spectral scheme used to solve equations (3.3, 3.4) for flow velocity components of u and v . This function takes velocity field, cylinders velocities and $\chi(\mathbf{x}, t)$ (mask) at each time step to calculate time derivatives for u and v . Function TREND2 (A.3) takes fluid forces (drag and lift), velocity

and displacement for each cylinder in the domain to compute the cylinder acceleration. In the main time stepping loop of the algorithm (A.1), time derivatives of \mathbf{u} , $\mathbf{U}_{\mathbf{o},i}$ and $\mathbf{X}_{\mathbf{o},i}$ calculated by TREND functions are integrated in time within four steps of Runge-Kutta method. At each time step, based the new values of $\mathbf{U}_{\mathbf{o},i}$ and $\mathbf{X}_{\mathbf{o},i}$, the collision equations will be solved if cylinders are hitting. This operation is performed by a function named *Impulse control*. Equations corresponding to each step of the main algorithm have been printed in the comments, to relate the mathematical model and numerical methods to the computational tool developed for this problem.

Here, we should point out the number of Fourier transforms needed to be performed in our algorithm. As can be seen in the main algorithm (1), in each Runge-Kutta step the pseudo-spectral scheme needs four forward and three backward transforms. Multiplying by four steps of Runge-Kutta, in total 28 Fourier transforms per time step are needed. In addition, the computational complexity of a 2-D Fourier transform using FFT algorithm is $O(N^2 \log(N))$, whereas computational complexity of algorithm (A.1) excluding Fourier transforms is $O(N^2)$. Consequently, the computational complexity is verified by complexity of the FFTW algorithm $O(N^2 \log(N))$. This shows the high cost of computation at each time step due to relatively high number of transforms and high computational costs for large problems. In the next chapter, we will discuss the algorithm efficiency and computational performance in detail.

```

begin
  initialize  $\rightarrow \mathbf{u}, \mathbf{X}_{o,i}, \mathbf{U}_{o,i}, mask$ ;
  add noise  $\rightarrow \mathbf{u}$ ;
  perturb  $\rightarrow \mathbf{X}_{o,i}$ ;
  while  $t \leq t_{end}$  do
    update  $dt \leftarrow \mathbf{u}$ ; /* 3.12,3.16 */
    for  $RK \leftarrow 1$  to 4 do
      update  $mask \leftarrow \mathbf{X}_{o,i}$ ; /* 3.5 */
       $\partial \mathbf{u} / \partial t \leftarrow \text{TREND1}(\mathbf{u}, \mathbf{U}_{o,i}, mask)$ ; /* 3.3, 3.4 */
       $\mathbf{u}^{new} \leftarrow \text{integrate } \partial \mathbf{u} / \partial t$ ; /* 3.15 */
      for  $i \leftarrow 1$  to  $Nc^2$  do
         $\text{Drag}_i$  and  $\text{Lift}_i \leftarrow \text{Calculate\_Force}(\mathbf{u}, \mathbf{U}_{o,i}, mask)$ ; /* 3.8 */
         $\partial \mathbf{U}_{o,i} / \partial t \leftarrow \text{TREND2}(\text{Drag}_i, \text{Lift}_i, \mathbf{U}_{o,i}, \mathbf{X}_{o,i})$ ; /* 3.9 */
         $\partial \mathbf{X}_{o,i} / \partial t \leftarrow \mathbf{U}_{o,i}$ ;
         $\mathbf{U}_{o,i}^{new} \leftarrow \text{integrate } \partial \mathbf{U}_{o,i} / \partial t$ ; /* 3.15 */
         $\mathbf{X}_{o,i}^{new} \leftarrow \text{integrate } \partial \mathbf{X}_{o,i} / \partial t$ ; /* 3.15 */
      end
      // based on 3.11, 3.12:
      For each  $i$ :  $\mathbf{U}_{o,i}^{new}, \mathbf{X}_{o,i}^{new} \leftarrow \text{Impulse control}(\mathbf{U}_{o,i}^{new}, \mathbf{X}_{o,i}^{new})$ ;
    end
     $t^{new} \leftarrow t + dt$ ;
  end
end

```

Algorithm 1: The main computational algorithm consist of initializations and a time loop containing Runge-Kutta time integration, TREND1 and TREND2.

```

Function TREND1(u, Uo,i, mask);

begin
     $\widehat{u} \leftarrow \text{FFT}(u)$  ;
     $\widehat{v} \leftarrow \text{FFT}(v)$  ;
     $\partial^2 \widehat{u} / \partial x^2 + \partial^2 \widehat{u} / \partial y^2 \leftarrow \widehat{u}$ ;
     $\partial^2 \widehat{v} / \partial x^2 + \partial^2 \widehat{v} / \partial y^2 \leftarrow \widehat{v}$ ;
     $\widehat{\omega} \leftarrow \partial \widehat{u} / \partial y, \partial \widehat{v} / \partial x \leftarrow \widehat{u}, \widehat{v}$ ;
     $\omega \leftarrow \text{iFFT}(\widehat{\omega})$ ;

     $\partial u / \partial t|_1$  and  $\partial v / \partial t|_1 \leftarrow u, v, \omega, \text{mask}, u_{o,i}, v_{o,i}$ ;
     $\partial \widehat{u} / \partial t|_1 \leftarrow \text{FFT}(\partial u / \partial t|_1)$ ;
     $\partial \widehat{v} / \partial t|_1 \leftarrow \text{FFT}(\partial v / \partial t|_1)$ ;
     $\partial \widehat{u} / \partial t|_2 \leftarrow \partial \widehat{u} / \partial t|_1 + \nu(\partial^2 \widehat{u} / \partial x^2 + \partial^2 \widehat{u} / \partial y^2)$ ;
     $\partial \widehat{v} / \partial t|_2 \leftarrow \partial \widehat{v} / \partial t|_1 + \nu(\partial^2 \widehat{v} / \partial x^2 + \partial^2 \widehat{v} / \partial y^2)$ ;

    if  $K_1^2 + K_2^2 == 0$  then
         $\begin{bmatrix} \partial \widehat{u} / \partial t \\ \partial \widehat{v} / \partial t \end{bmatrix} \leftarrow 0$  ; /* Fixed mean velocity */
        // Orthogonal projection on divergence free plane:
        else  $\begin{bmatrix} \partial \widehat{u} / \partial t \\ \partial \widehat{v} / \partial t \end{bmatrix} \leftarrow 1 / (K_1^2 + K_2^2) \begin{bmatrix} K_2^2 & -K_1 K_2 \\ -K_1 K_2 & K_1^2 \end{bmatrix} \begin{bmatrix} \partial \widehat{u} / \partial t|_2 \\ \partial \widehat{v} / \partial t|_2 \end{bmatrix}$  ;
    end

     $\partial u / \partial t \leftarrow \text{iFFT}(\partial \widehat{u} / \partial t)$ ;
     $\partial v / \partial t \leftarrow \text{iFFT}(\partial \widehat{v} / \partial t)$ ;

end

```

Algorithm 2: TREND1. This function describes the algorithm of pseudo-spectral scheme and orthogonal projection for divergence free condition.

```
Function TREND2(Dragi, Lifti, Uo,i, Xo,i);  
begin  
  | for i ← 1 to Nc2 do  
  |   | // based on 3.9:  
  |   |  $\partial u_{o,i}/\partial t \leftarrow (\text{Drag}_i - b u_{o,i} - k x_{o,i}) / (m + m_A);$   
  |   |  $\partial v_{o,i}/\partial t \leftarrow (\text{Lift}_i - b v_{o,i} - k y_{o,i}) / (m + m_A);$   
  | end  
end
```

Algorithm 3: TREND2. This function solves mechanical vibration equations using fluid forces, cylinder position and velocity to calculate acceleration of cylinders.

Chapter 4

High Performance and Parallel Computation

As discussed in the first chapter, we are investigating the possible effect of Reynolds number on instability of cylinders. For more complete analysis a wide range of Reynolds number should be simulated, ideally a range between 10^2 to 10^5 . It was indicated in the previous chapter that number of grid points is a function of Reynolds number ($N \geq C\sqrt{Re}$); therefore, for high Reynolds numbers, we need to compute a large and stiff numerical problem which needs 28 Fourier transforms per time step. The computational load of such problems has been an important issue for many investigators, since this is a direct numerical simulation (DNS) of a turbulent flow, with no turbulence modeling.

We chose C++ for programming because of its high speed as a low level language and ease of use compared to other low level static languages, C and Fortran. Our strategy to solving such a large sized problem is parallel processing, since serial execution takes unreasonable time of up to several months. Therefore we parallelized

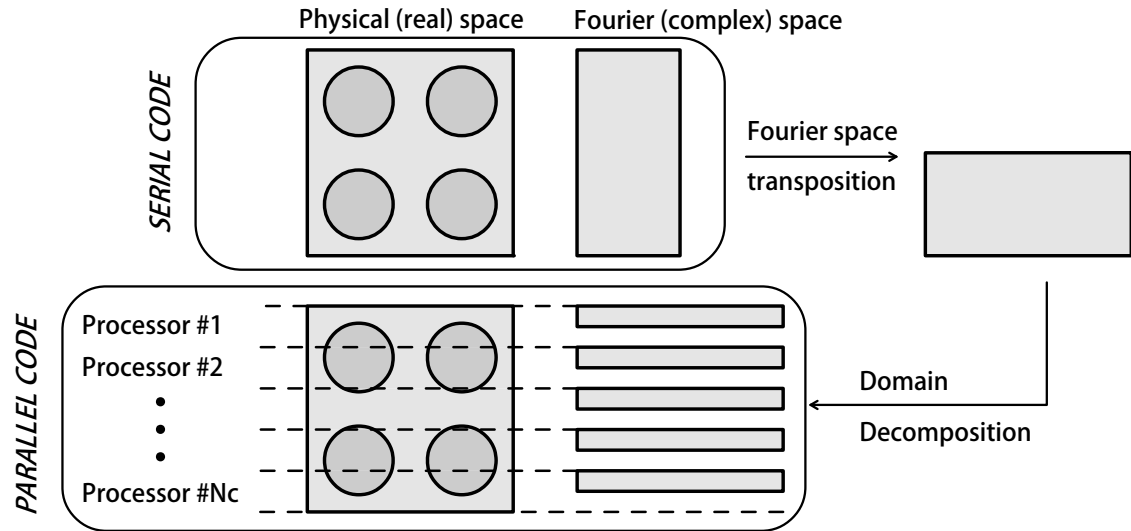


Figure 4.1: Domain decomposition for distributed parallel processing

the code using *Message Passing Interface* (MPI) to scale the computation on large number of processors. For distributed processing, the computational domain is decomposed among processors as figure (4.1) indicates. For higher efficiency and better load balancing, we use processors such that grid points are dividable by the number of processors.

Although parallel processing helps to speed up the computation, the equations stiffness issue is not resolved. At least, we have optimized the code and the algorithm to a high level to decrease the CPU time needed for each time step. Three steps have been taken for the code optimization:

- **Optimizing C++ and MPI:** We optimized our code using different steps. We decreased memory size to a level that does not affect the efficiency. The memory access is sequential and cache friendly aligned. We have also decreased

synchronizations and communications among processing units to lower communication overheads. Finally, $-O_i$ flags of auto optimization were used for compiling the code.

- **Fast Fourier Transform:** For the discrete Fourier transforms, we used the latest version of FFTW package (Version 3.3.4), which is one of the best and most reliable written packages for fast Fourier transforms [15]. It is mostly written in C language, which is well compatible with C++. The FFTW implementation gives many features for optimization at different levels. We skip the details and mention only two of the main optimization tactics. The first is the auto-tuning feature of FFTW, which allows the programmer to easily choose the best optimizing level. The cost of optimization for the programmer is negligible and for the code execution is usually a couple of seconds spent on hardware tests before the first Fourier transform execution. The second step taken to optimize FFTW was transposing the domain in Fourier space. The reason is that intermediate steps of FFTWs algorithms requires transposing the array and redistributing the data among CPUs. But by transposing the complex Fourier space, FFTW's algorithm avoids a global transposition for each transform [15]. Although rewriting the code is not always convenient for the programmer, this action is highly recommended. We achieved for our problem a speed up of ~ 1.5 to ~ 1.9 for different problem sizes.
- **Adaptive time stepping:** Time stepping was analyzed in detail before, and it was mentioned that for this specific problem, time step size is a function of time. Figure (4.2) suggests how time step size could be calculated based on stability and accuracy criteria in time. A conservative approach would be a

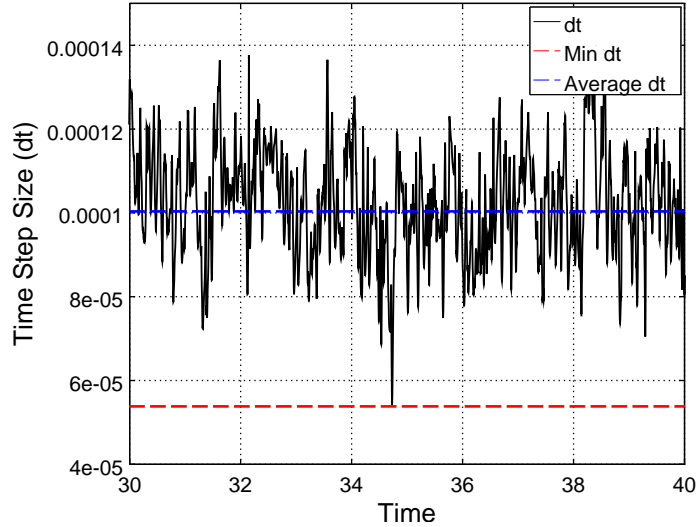


Figure 4.2: Time step size as a function of time (adaptive time stepping).

fixed size time stepping based on the most restrictive criterion, but consequently the total number of time steps increases. By taking the advantage of adaptive time stepping, the average time step size increases which leads to less time steps and computation in total. This optimizing strategy, gives about 1.8 to 2 times speed up (for case of figure 4.2 it is exactly 1.87), while the desired accuracy is achieved.

In summary, by optimizing the code we achieved the total speed up of about 3-4.5 for the serial version of the code. The achieved speed up for the parallel code is also considerable. In order to verify the parallelism efficiency we use strong and weak scaling methods. The strong scaling is calculated by

$$\text{Strong Scaling Efficiency} = \frac{T_1}{N_p T_2} \times 100\%$$

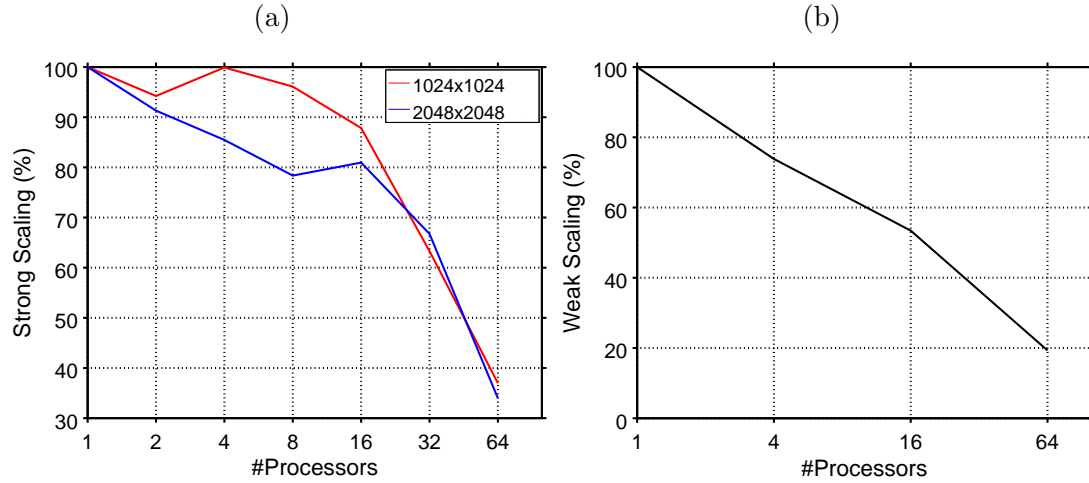


Figure 4.3: (a) Strong scaling for 2048×2048 and 1024×1024 problem sizes, (b) weak scaling for a fixed problem size of 256×256 per processor.

and weak scaling by

$$\text{Weak Scaling Efficiency} = \frac{T_1}{T_2} \times 100\%$$

where N_p is number of processing unit, T_1 and T_2 are CPU times for serial and parallel executions, respectively. The total problem size is fixed for strong scaling; in contrast, the problem size increases linearly by number of processors for case of the weak scaling, while the work load per processor is fixed¹.

Figures 4.3a and 4.3b suggest strong and weak scaling parallelism efficiencies, respectively. In the figure (4.3a) it is evident that up to 16 CPUs parallelism efficiency is relatively high (more than 80%); but the efficiency decreases when we use CPUs more than 16. In order to interpret this behavior, we need to consider the computation

¹Source: www.sharcnet.ca

in terms of hardware and software. The FFTW algorithm needs global communication between CPUs. Therefore global synchronizations are essentially required. This affects the parallelism efficiency and increases communication overhead. The weak scaling of figure (4.3b) helps to better understand this behavior, since it clearly suggests that each processor needs more time to finish a fixed amount of work when number of processors increases. This means the communication is the bottleneck for parallel FFTW implementation. The interesting data is that the performance remains high up to 16 cores. This is because the machine that we used for executions is consist of 4×16 -core CPUs, and 16 CPUs are connected by a shared memory and communication in a shared memory system is a lot faster than distributed memory architecture.

Overall, by parallel computing up to 24 times speed-up was achieved, which is very important and crucial for simulating the problem at high Reynolds numbers. In order to give an estimation on CPU time, simulation of a high resolution problem of size 2000×2000 at the mean flow velocity of $U = 2$ and Reynolds number of $Re_g = 60,000$ for 20 time units (non-dimensional scale) takes ~ 65 days using a single core² (figure: 4.4). This could be reduced to 2.7 days using 64 cores which is noticeable and pretty much acceptable time for a direct numerical simulation of high Reynolds turbulent fluid flow problem.

In summary, we successfully developed an efficient high performance computational tool to simulate the flow past an array of moving cylinders using a highly accurate pseudo-spectral method. The code efficiency allows us to simulate the problem for Reynolds numbers of up to 100,000 at a reasonable time. This was our starting

²CPU: AMD Opteron(tm), processor id: 6378, 2.4 GHz, 2048 KB cache

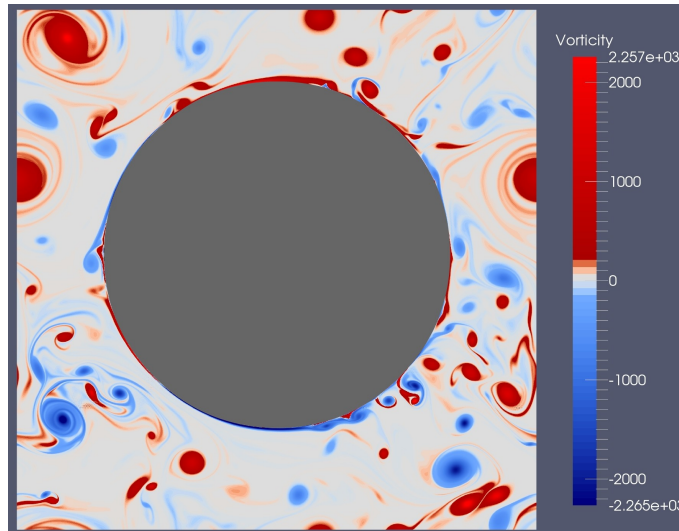


Figure 4.4: High resolution flow simulation (vorticity field at $Re_g = 60,000$).

point to uncover the role of Reynolds number in the onset of fluid-elastic instability. In the next chapter we will present our numerical results achieved by extensive simulations of the problem.

Chapter 5

Simulation Results and Discussion

In chapters 3 and 4, we presented the mathematical model, the numerical method, the algorithm and the computational tool for solving this problem. Therefore, almost everything needed for simulation has been described. Now, in this chapter, we are going to present and discuss the simulation results performed to uncover the role of Reynolds number in the onset of fluid-elastic instability. As discussed earlier, simulations are expensive for high Reynolds numbers. So it is crucial to choose key parameters of the problem such that we would be able to capture the desired results using less computations. Otherwise waste of time and resources is inevitable. At this point it is helpful to recall chapter 1 and 2 where we discussed the physics of the problem, since we assume the simulation results are close to the experimental measurements.

5.1 Basic parameters of the simulation

We consider two cases: in-line and rotated (staggered) square arrays with pitch-to-diameter ratio of 1.5 (see figure: 1.1) and start with case of fixed cylinders case to obtain preliminary insights on the case of moving cylinders and instability occurrence. We put $N_c = 2$ (2×2 cylinders per periodic domain) since anti-phase oscillation between rows/columns is not possible for the case of a single cylinder per periodic domain. We have also observed that two cases of $N_c = 2$ and 3 are consistent in terms of vortex shedding and Strouhal number for the fixed cylinder case. We are also interested to simulate the problem for as wide a range of Re numbers as we can afford. Considering the time and the available resources we chose a range of 300 to 9600 (in-line) and 210 to 6800 (rotated) for Re_g to analyze turbulence level effects.

Since our focus is the onset of fluid-elastic instability, using the Blevins experimental results (see figure: 2.3) we set up the parameters such that lock-in phenomenon (resonant excitation) does not occur or interfere the self-excitation of cylinders. Considering all the discussed factors, for each of the simulations we set Scruton number $Sc = 0.8$ and natural frequency $f_N = 1.0$. In this way the range of flow velocities where lock-in occurs is fixed and far enough from fluid-elastic vibrations (see figure: 2.4d). A Sc of 0.8 is relatively low compared to the range of 0.01 to 16.0 in the previous investigations; this is because we want cylinders to oscillate easily and become unstable in lower flow velocities. And also it should be mentioned that all parameters are non-dimensional which means we assume the size of cylinder and density of the fluid to be one ($D = 1$, $\rho = 1$).

Before going further, it is important to discuss the critical flow velocity and define

the critical point. We mentioned in chapter 2 that the cylinders oscillation amplitude increases dramatically if the fluid velocity exceeds a critical threshold, in case of fluid-elastic instability. In fact, there is no universal definition of critical velocity. Therefore, in order to clearly define the critical point, we consider Y_{rms}/D of 12% and 10% for in-line and rotated arrays respectively, where Y_{rms} is the RMS value of cylinder response in transverse flow direction. The reason we define different values for critical point is due to the different types of responses in different cylinder configurations. This will be discussed later in more details.

It is important to point out the duration of the simulation. Generally, higher simulation time interval give better converged results but the CPU time increases proportionally. Therefore, this parameter should be set carefully. We stop simulations at T_{end} once the fluid flow regime is fully developed and cylinder responses are converged to statistically steady state solutions. Our definition of T_{end} is the state in which RMS value of cylinder responses¹ are converged. This is a useful and inexpensive criterion since it also implies the flow is fully developed. T_{end} is therefore not a fixed parameter and is defined separately for each simulation.

5.2 Reynolds number and Strouhal number

We start our simulations with the case of four fixed cylinders per periodic domain, since this case helps us to better analyze fluid behavior for the cases in which cylinders are free to move. Figure (5.1) shows the frequency spectrum of the non-dimensional lift force (C_L) for one of the cylinders in a in-line and in a staggered array at different Reynolds numbers. There are important facts about these plots that we need to

$$^1Y_{RMS} = \sqrt{\frac{\sum y_k^2}{Time\ steps}}$$

consider when discussing Reynolds number effect.

At $Re_\infty \leq 200$ (figures: 5.4a, 5.4b) we observe a sharp dominant frequency corresponding to strong vortex shedding in the rotated array and the lift force amplitude is also large. This is because flow is highly laminar and structured. For the in-line array, the lift force amplitude is relatively small because vortex shedding does not occur completely and the flow is jet like. At $Re_\infty \geq 400$ (figures: 5.4c, 5.4d and 5.4e), we see the flow becomes unstable and the lift force frequency bandwidth increases considerably. The higher the Reynolds number, the wider the frequency spectrum and the stronger the vortex shedding. Although this is not unexpected because of the nature of flow for low viscosity fluids, the important fact to be noticed is the transition region. The turbulence level in cylinder arrays due to a high level of fluid-solid interaction is great. This implies that even at moderate Reynolds numbers the flow becomes unstable. In summary, there are two distinct flow regimes, one is regular and structured ($Re_\infty \leq 200$) and the other is unstructured and has complex (turbulent) behavior ($Re_\infty \geq 400$).

For the final part of this section, we validate our simulations by comparing the Strouhal numbers with the experimental measurements given in the figure (5.2) for the rotated array. As it can be seen, although the experiment has been performed for a finite non-periodic array, the simulation results for Strouhal numbers compare well with the experimental data. Also for the case of the in-line array, figure (2.2) in chapter 2 gives $St = 0.34$ (or 1.02 based on up-stream flow velocity) for $P/D = 1.5$ at an unknown Reynolds number [13] which is comparable with the numerical results: $St = 0.366$ at $Re_\infty = 200$ (5.1b) and the dominant normalized frequency of $St = 0.326$ at $Re_\infty = 400$ (5.1c).

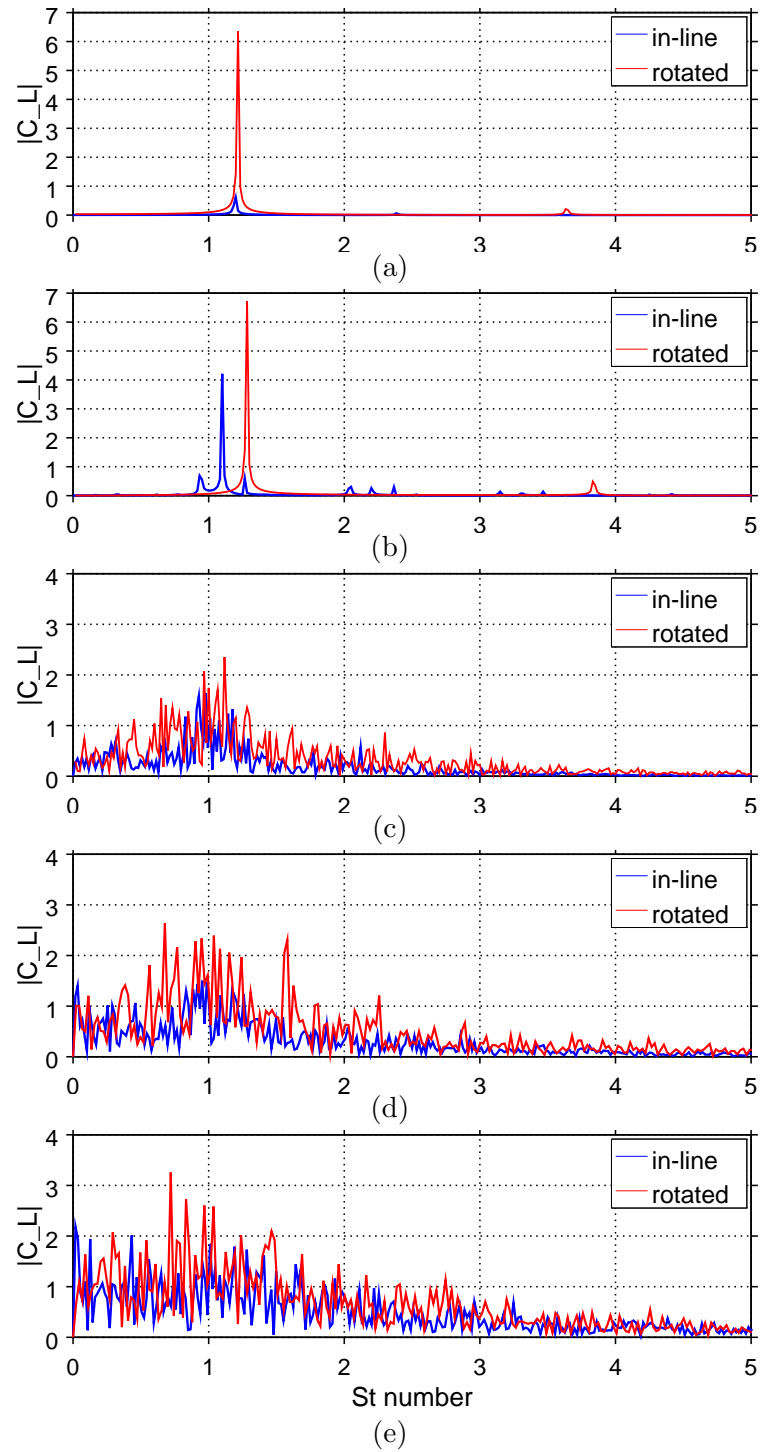


Figure 5.1: Lift force (C_L) frequency spectrum at (a) $Re_\infty = 100$ (b) $Re_\infty = 200$ (c) $Re_\infty = 400$ (d) $Re_\infty = 800$ (e) $Re_\infty = 1600$ [upstream flow velocity based], for fixed in-line and rotated arrays.

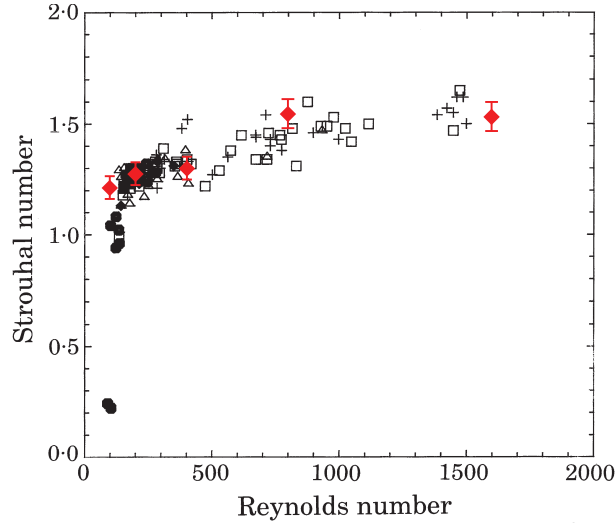


Figure 5.2: Modified plot of Strouhal number versus Reynolds number in rotated square array (Price, Paidoussis and others, 1995) [25]. Black symbols correspond to experimental measurements for different rows in the array and added red diamond signs denote to the simulation results.

5.3 Effect of Reynolds number on fluid-elastic instability in an in-line square array

In the present and the following sections, we present the main results of our study. Our strategy to uncover the effect of Reynolds number on critical flow velocity is to simulate the flow through moving cylinder arrays, for a wide range of Reynolds numbers (considering the time and available computing resources) and at a range of flow velocities in which fluid elastic instability occurs. In other words, we independently vary flow velocity and Reynolds number at a fixed Scruton number of $Sc = 0.8$. We already mentioned that in order to avoid interference of resonant in non-resonant instabilities, the parameters are chosen in a way that synchronization (lock in) does not occur. In this part, we discuss the results for in-line square array.

The contour plot (5.3a) illustrates the RMS values of cylinder vibrations in transverse flow direction as a function of Reynolds number and reduced flow velocity for fixed Scruton number of 0.8, in which small black circles correspond to simulation results. The expressed RMS values are the average RMS values for all cylinders in the domain. Lines 1 and 2 denote to the mean and lower bound on critical reduced flow velocities, based on the information in table (2.1) and the Blevins experiments (figure: 2.3), for in-line configuration, $P/D=1.5$ and $Sc = 0.8$. It is important to note that neither references indicate the Reynolds number range in which they are supported to be valid.

Therefore, we performed 36 simulations, covering a considerable range of flow velocities beyond the lower bound (line 2) and close to the onset of fluid-elastic instabilities, for Reynolds numbers of 300 to 9600. There are some important facts that we can observe from the simulation results for the in-line case. First, a relatively sharp increase in oscillation amplitudes near line 1 divides the graph into stable and unstable regions. This is consistent with the physics of fluid-elastic instability that we discussed in section 2.2 . The sudden change in RMS values which is referred to as the critical point also fluctuates around and then converges to line 1 at high Reynolds number, which is a good criterion to validate our simulations.

Although the critical velocity is generally close to line 1 and converges to that line at $Re_g \geq 4800$, we observe that increasing the Reynolds number from 600 to 1200 alters the onset of instabilities considerably. In other words, the cylinders are more stable at $Re_g = 600$ than they are at either $Re_g = 300$ or $Re_g = 1200$. In order to better understand this phenomenon, it is helpful to take a closer look at the flow. Figure (5.4) shows the vorticity fields at different Reynolds numbers. We observe that

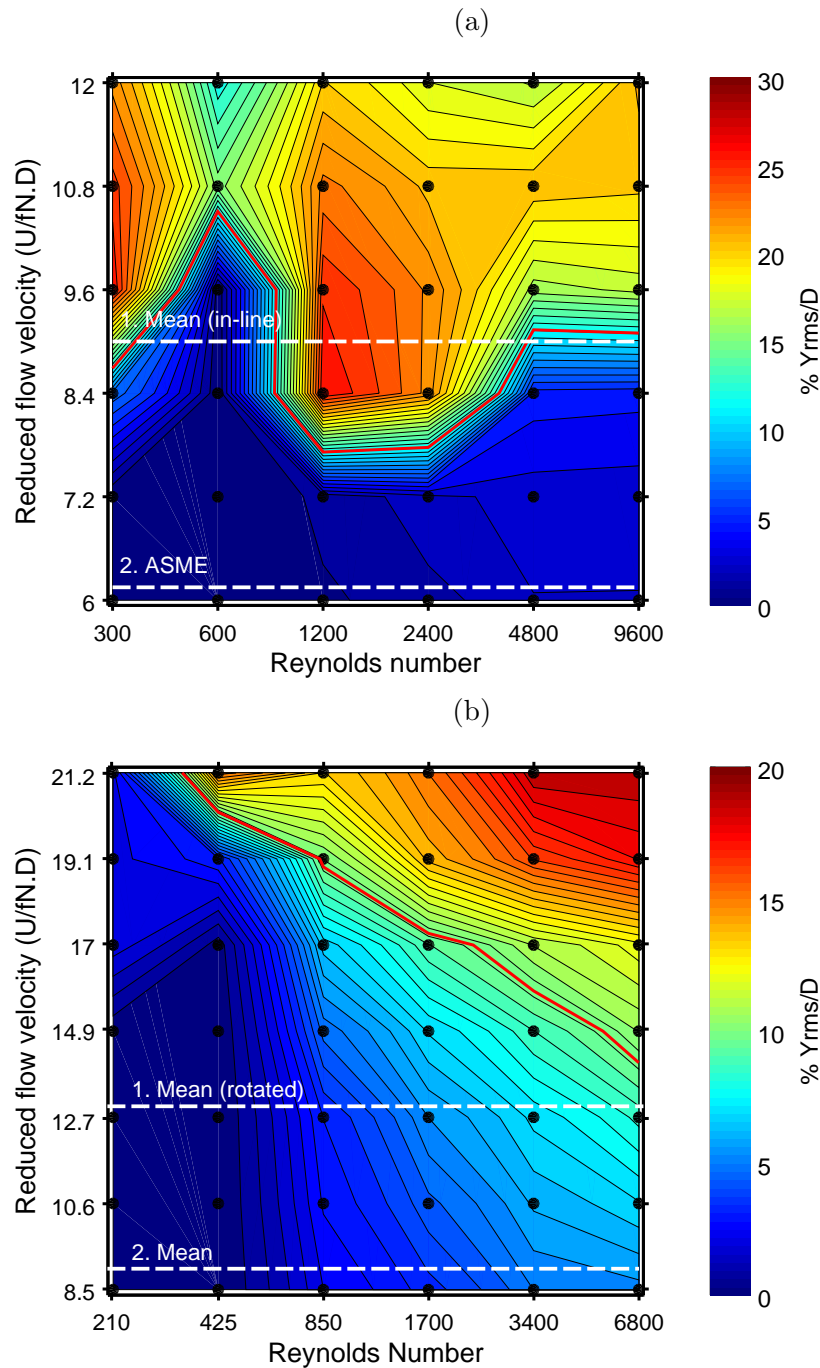


Figure 5.3: Onset of fluid-elastic instability as a function of Reynolds number and reduced flow velocity in (a) the in-line square array (b) the staggered square array. Based on experimental results, in figure (a) lines 1 and 2 correspond to the mean and lower bound on critical flow velocities, respectively. In figure (b) lines 1 corresponds to the mean critical flow velocities for different geometries and line 2 for the rotated array.

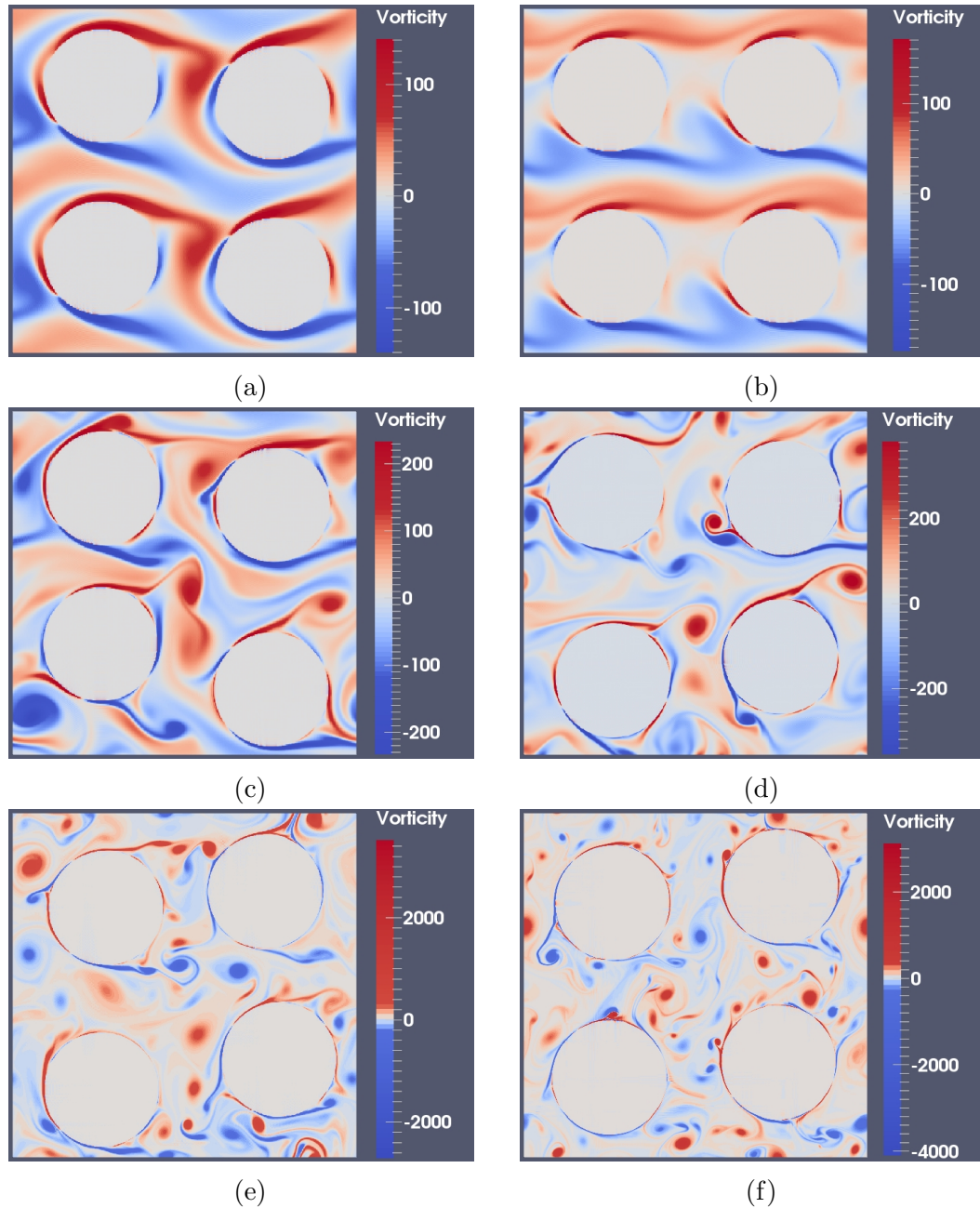


Figure 5.4: Vorticity fields at (a) $Re_g = 300$, (b) $Re_g = 600$, (c) $Re_g = 1200$, (d) $Re_g = 2400$, (e) $Re_g = 4800$, (f) $Re_g = 9600$, for moving in-line cylinder array subjected to cross flow at $U_g = 9.0$.

the flow at $Re_g = 600$ has a regular and wavy jet like structure when passing through cylinders. This particular wavy wake does not occur in other Reynolds numbers, and might be the main reason for enhanced stability since the flow structure conforms to the cylinder array. Interestingly, even the unstable region at $Re_g = 600$ has a lower vibration amplitude than the other Reynolds numbers. So, if the flow structure and geometry of the array at this Reynolds number have a stabilizing effect, the question is what effect geometry or array spacing can have on the critical velocity. To find a quick answer to this question, we performed other simulations by keeping the same reduced gap velocity, Scruton and Reynolds numbers and varying the pitch-to-diameter ratio from 1.4 to 2.0. As figure (5.5) illustrate, the simulation results confirm that the onset of fluid-elastic instability is sensitive to the array spacing in the in-line case, since a slightly tighter packing ($P/D=1.4$) produces instability whereas looser packings ($1.5 \leq P/D \leq 2.0$) are stable. Therefore, we can attribute the higher stability of the problem at $Re_g = 600$ to the conformity of the fluid flow structure with the array geometry. At this point, more in-depth study would be helpful to better understand the effect of array spacing on critical flow velocity and is considered for future work.

5.4 Effect of Reynolds number on fluid-elastic instability in a staggered square array

After the in-line case, we consider rotated arrays with the same Scruton number (Sc) and pitch-to-diameter (P/D). We performed 42 simulations for different flow velocities to investigate how the instability threshold changes with Reynolds numbers. The

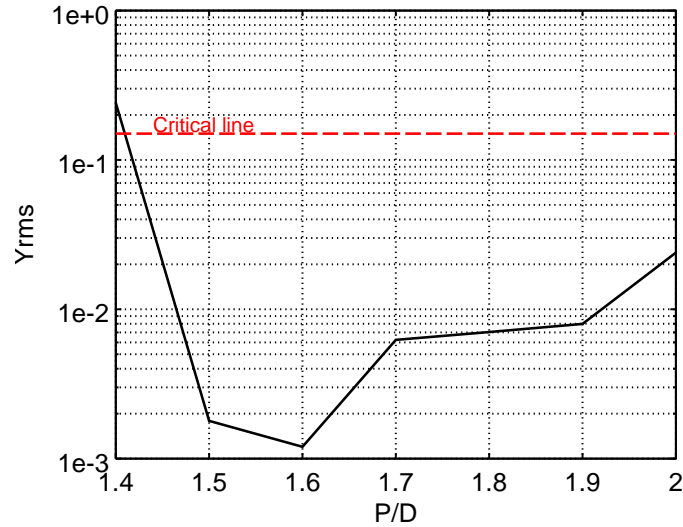


Figure 5.5: Cylinder response as a function of pitch-to-diameter (P/D) in the in-line array with fixed gap flow velocity of 9.0 and Reynolds number of $Re_g = 600$. Critical line denotes to the critical point using Blevins experimental data (see figure: 2.3).

contour plot (5.3b) shows the simulation results (black circles) as RMS of cylinder response to the flow in the transverse flow direction as a function of reduced gap velocity and Reynolds number. The RMS values are the average values for all cylinders in the domain. Line 2 corresponds to the mean values of critical flow velocity for different geometries (see figure 2.3) while line 1 denotes to the experimental values for exclusively rotated arrays in the same graph.

As figure (5.3b) suggests, it is clear that in contrast to the in-line array, vibration amplitude increases very smoothly with both the flow velocity and Reynolds number. This behavior is due to the cylinders' geometry and the structure of the flow since, regardless of the flow velocity, the fluid has to pass through the cylinder array by changing its direction frequently, causing a higher level of interaction between fluid and solid (figure: 5.6). In this case, even at stable regions, we observe some random oscillations in which the amplitudes increase with increasing the Reynolds number

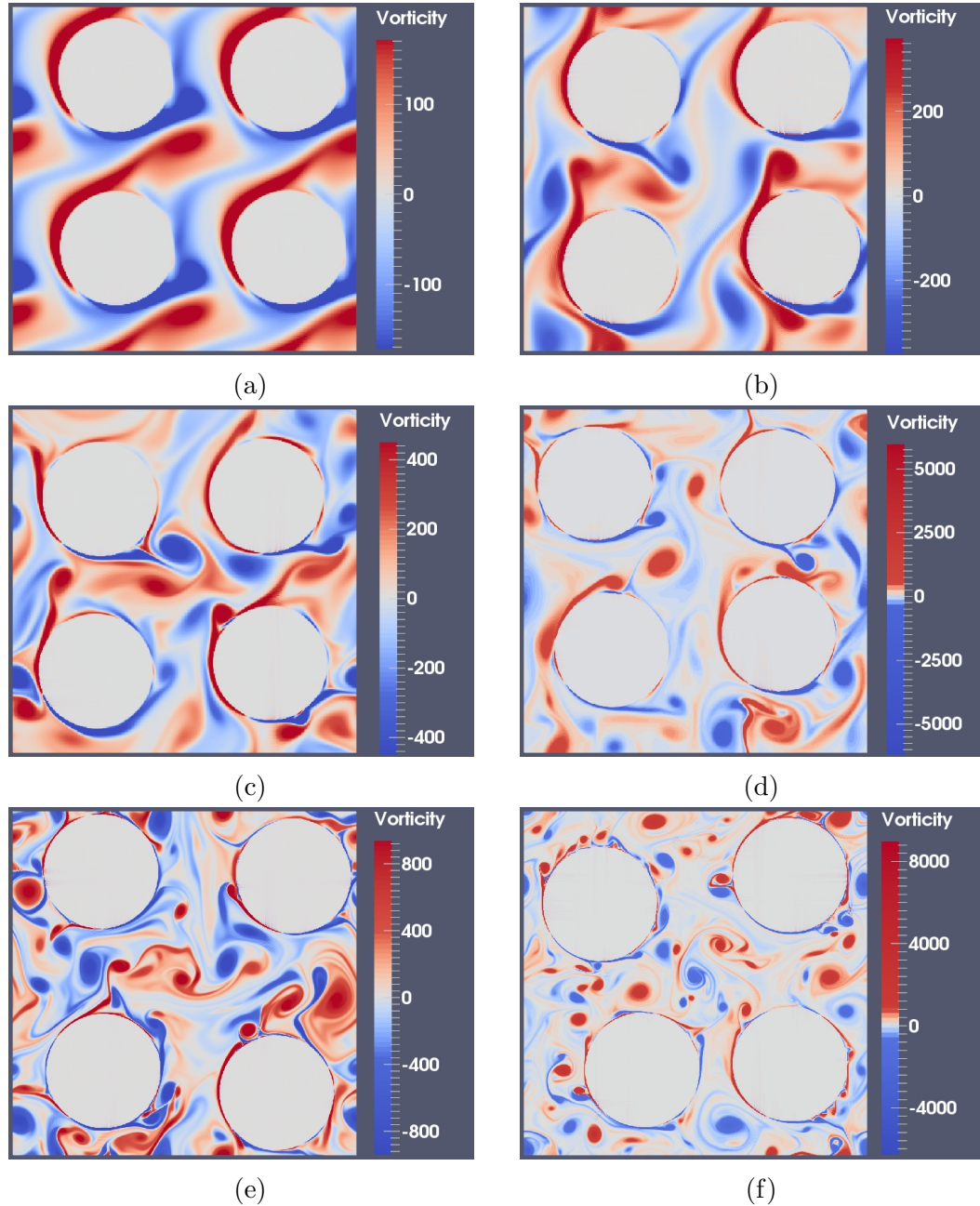


Figure 5.6: Vorticity fields at (a) $Re_g = 210$, (b) $Re_g = 425$, (c) $Re_g = 850$, (d) $Re_g = 1700$, (e) $Re_g = 3400$, (f) $Re_g = 6800$, for moving rotated cylinder array subjected to cross flow at $U_g = 21.2$.

due to the turbulence buffeting effect.

The most important information in the figure (5.3b) is how critical velocity changes with the Reynolds number in the rotated array. The Reynolds number effect in staggered arrays is much more significant than the in-line case, since the instability threshold decreases down to half of flow velocity when the Reynolds number (Re_g) changes from 210 to 6800. In other words, the critical velocity decreases monotonically with increasing Reynolds number and turbulence level. In this case, we identify the turbulence buffeting effect as a de-stabilizing factor for the cylinder vibrations. Compared to line 1, we see that the critical point appears to approach line 1 and probably will converge to a line between line 1 and 2, if we simulate the problem to higher Reynolds number than 6800. This is actually a very important result since we have untangled the significance of the Reynolds number effect on fluid-elastic instability for in-line and staggered arrays. It is appropriate at this point to highlight that all the previous experimental data, as well as theories, have ignored the Reynolds number effect or have reported it as an unclear factor.

5.5 Discussion

Analyzing flow-induced vibrations in the in-line and the staggered array, reveals some important differences. The flow visualizations (figures: 5.4, 5.6) and lift frequency spectra (figure: 5.1) suggest that the vortex shedding in the staggered array is very strong independent of Reynolds number. On the other hand, for the in-line array the flow has more jet like structure and vortex shedding is not complete at low Reynolds number. Small vortices are shed at higher Reynolds numbers which cause turbulence buffeting. This effect can be seen in figure (5.3a) at the stable region in which

oscillation amplitudes are small.

Additionally, comparing figures (5.3b) and (5.3a), we observe that the onset of fluid-elastic instability in the in-line array is sharp respect to a small increase in the flow velocity. In contrast, in the staggered array vibration amplitudes increase smoothly and monotonically with both flow velocity and Reynolds number. Responses in these two configurations are also deferent. Figures (5.7a, 5.7b) show typical responses and histogram of cylinder position for in-line and staggered arrays with the same Y_{rms}/D values of 20%. Compared to a sine function, we observe responses in in-line arrays (at unstable region) are more similar to sine waves in which vibration amplitudes are slightly changing over time. On the other hand, for rotated array vibration amplitudes varies from zero to a relatively high values. This leads to a higher maximum oscillation amplitudes in staggered compared to in-line arrays, with the same Y_{rms}/D values. That is why we choose lower RMS value (10% instead of 12%) for defining critical point in rotated array case.

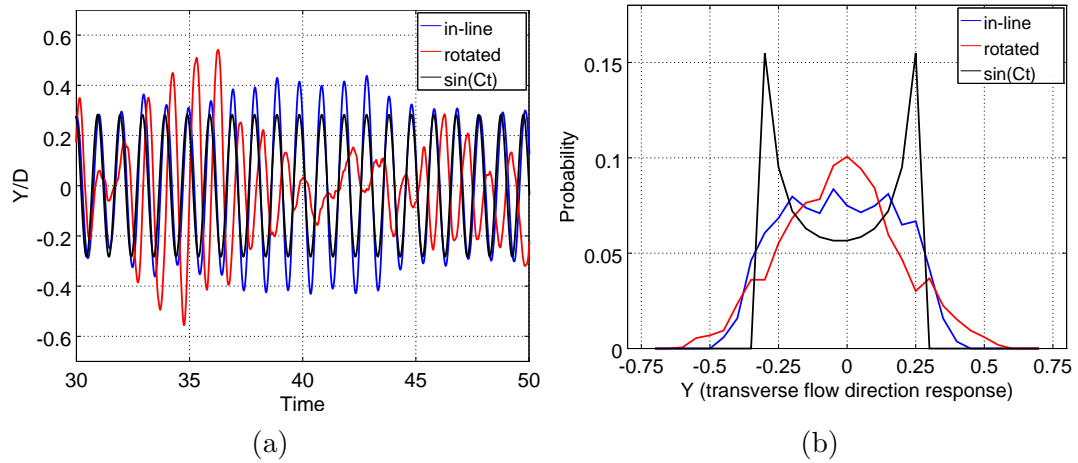


Figure 5.7: (a) Cylinder response at unstable regions for an in-line and a staggered array compared to a sine function with equal RMS values. (b) The corresponding histogram of cylinder positions for the same cylinder arrays, compared to sine function.

Chapter 6

Conclusions and Outlook

In this study, we presented the mathematical model, the numerical method and the computational algorithm, developed and applied to efficiently and accurately simulate the flow-induced vibrations in a periodic cylinder array and therefore investigate the effect of Reynolds number effect on the onset of fluid-elastic instability. We performed roughly 0.5 million CPU-hour simulations using a local 128-core machine¹ and SHARCNET computing resources², to find convincing evidence in order to untangle the controversial role of Reynolds number in critical flow velocity for fluid-elastic instability.

As discussed in the previous chapters, we have successfully developed an efficient and high performance parallel code to numerically simulate this complicated problem and demonstrated that our simulation results are consistent with experimental results. After we verified the code, we performed extensive computations to investigate whether Reynolds number has stabilizing or destabilizing effect on fluid-elastic

¹IF and ORME

²ORCA and SAW

vibrations independent of cross flow velocity. We found that in a rotated square array cylinders are highly stable at low Reynolds numbers; however the critical flow velocity decreases significantly at higher Reynolds numbers, which is consistent with the data of Franklin and Soper (1977) [14]. This evidence certainly improves our understanding of this phenomenon and suggests that investigators should include Reynolds number as the third parameter to predict the critical flow velocity. We performed similar simulations for an in-line array and we found a relatively weak effect of Reynolds number on instabilities, which is inconsistent with the experimental measurements of Southworth and Zdravkovich (1975) [29].

Comparing our numerical simulation results with the Blevins experiments (see figure:2.3), we see our prediction of the onset of fluid-elastic instability is very close to the experimental measurements, for the in-line array case in which we showed the Reynolds number effect is weak. On the other hand, the simulation results demonstrated higher critical flow velocity than the Blevins measurements for the staggered array in which Reynolds number effect is strong. In the range of $Re_g = 210 - 6800$, we showed that the critical flow velocity monotonically decreases with Reynolds number and approaches to the Blevins experimental measurements for the staggered array case. Here, we conclude the Blevins experiments have been performed at a Reynolds number higher than 6800 and consequently, this can help to find out the origin of the uncertainty in experimental data.

The comparison of these two simulation series for the in-line and the rotated array demonstrates the strong role of geometry in instabilities, together with Reynolds number. The highly stable low Reynolds number region of the rotated array and the instability of the in-line array at low Reynolds numbers invalidates the Blevins claim

that the geometry of the array has a weak effect on instabilities [5]. In addition, the simulation results and the flow visualizations showed different wake regions and vortex shedding mechanisms of the staggered array compared to the in-line array. Therefore we conclude that the effect of array geometry and Reynolds number on the fluid-elastic instability are both considerable and intrinsically dependent. This is because turbulence level, fluid forces and vortex shedding are affected by these two parameters, independent of cross flow velocity.

Finally, it is important to highlight the fact that our simulation results are based on a limited range of Reynolds numbers, specific geometries and a fixed Scruton number. We also modeled a two dimensional, incompressible, single phase and steady flow. Therefore, in order to make a definite conclusion about the role of Reynolds number on fluid-elastic instability, we should extend our numerical experiments. Another case which can help us to better understand the role of turbulence in this problem is simulating the fluid flow in a non-periodic cylinder array (e.g. a tube array in channel flow). Simulating a non-periodic finite sized tube bundle is slightly different from reality, though consistent with the previous experimental measurements. In this case, by using a turbulence generator at the inlet we would be able to control turbulence intensity for a fixed Reynolds number. All of these ideas are considered for future steps and are contingent on the available time.

Bibliography

- [1] Angot, P., Bruneau, C.-H., and Fabrie, P. (1999a). A penalization method to take into account obstacles in incompressible viscous flows. *Numerische Mathematik*, **81**(4), 497–520.
- [2] Angot, P., Bruneau, C.-H., and Fabrie, P. (1999b). A penalization method to take into account obstacles in incompressible viscous flows. *Numerische Mathematik*, **81**(4), 497–520.
- [3] ASME (1995). *ASME Boiler and Pressure Vessel Code*. ASME. Section III Rules for Construction of Nuclear Power Plant Components Division 1 - Appendices.
- [4] Blevins, R. (1984). *Journal of Sound and Vibration*, **92**(4), 455–470.
- [5] Blevins, R. D. (2001). *Flow-induced vibration*. Krieger Publishing Company, second edition.
- [6] Carbou, G., Fabrie, P., *et al.* (2003). Boundary layer for a penalization method for viscous incompressible flow. *Advances in Differential equations*, **8**(12), 1453–1480.
- [7] CHEN, S. (1978). Crossflow-induced vibrations of heat exchanger tube banks. *Nuclear Engineering and Design*, **47**.

-
- [8] Chen, S. (1987a). *Flow-Induced Vibration of Circular Cylindrical Structures*. Hemisphere Publishing Corporation, Washington.
- [9] Chen, S.-S. (1987b). Flow-induced vibration of circular cylindrical structures.
- [10] Chen, S. S. and Jendrzejczyk, J. A. (1981). Experiments on fluid elastic instability in tube banks subjected to liquid cross flow. *Sound and Vibration*, **78**.
- [11] Chen, Y. (1968). Flow-induced vibration and noise in tube-bank heat exchangers due to von karman streets. *Journal of Manufacturing Science and Engineering*, **90**(1), 134–146.
- [12] Connors, H. J. (1970). Fluidelastic vibration of tube arrays excited by cross flow. Paper presented at the Symposium on Flow Induced Vibration in Heat Exchangers.
- [13] Fitzhugh, J. (1973). Flow induced vibration in heat exchangers. Report RS57 (AERE P7238).
- [14] Franklin, R. and Soper, B. (1977). An investigation of fluidelastic instabilities in tube banks subjected to fluid cross-flow. In *Structural mechanics in reactor technology*.
- [15] Frigo, M. and Johnson, S. G. (2003). FFTW users manual. *Massachusetts Institute of Technology*.
- [16] Kevlahan, N. K.-R. and Ghidaglia, J.-M. (2001). Computation of turbulent flow past an array of cylinders using a spectral method with brinkman penalization. *European Journal of Mechanics-B/Fluids*, **20**(3), 333–350.

- [17] Kevlahan, N.-R. and Wadsley, J. (2005). Suppression of three-dimensional flow instabilities in tube bundles. *Journal of fluids and structures*, **20**(4), 611–620.
- [18] Lever, J. and Weaver, D. (1982). A theoretical model for fluid-elastic instability in heat exchanger tube bundles. *Journal of Pressure Vessel Technology*, **104**(3), 147–158.
- [19] MacDonald, P. E., Shah, V., Ward, L., and Ellison, P. (1996). Steam generator tube failures. Technical report, Nuclear Regulatory Commission, Washington, DC (United States). Div. of Safety Programs.
- [20] Meriam, J. L. and Kraige, L. G. (2013). *Engineering mechanics: Dynamics*. John Wiley & Sons, seventh edition.
- [21] Mewes, D. and Stockmeier, D. (1991). Fluid viscosity effects on flow induced vibrations of tube bundles in cross-flow. In *Proceedings of 5th International Conference on Flow Induced Vibrations, Brighton*, pages 231–242.
- [22] Nakamura, T., Kaneko, S., Inada, F., Kato, M., Ishihara, K., Nishihara, T., and Mureithi, N. W. (2013). *Flow-induced vibrations: Classifications and lessons from practical experiences*. Butterworth-Heinemann.
- [23] Paidoussis, M. P., Price, S. J., and de Langre, E. (2010). *Fluid-structure interactions: Cross-flow-induced instabilities*. Cambridge University Press, first edition.
- [24] Price, S. and Paidoussis, M. (1984). An improved mathematical model for the stability of cylinder rows subject to cross-flow. *Journal of Sound and Vibration*, **97**(4), 615–640.

- [25] Price, S., Païdoussis, M., Mark, B., *et al.* (1995). Flow visualization of the interstitial cross-flow through parallel triangular and rotated square arrays of cylinders. *Journal of Sound and Vibration*, **181**(1), 85–98.
- [26] Roberts, B. W. (1966). Low frequency, aeroelastic vibrations in a cascade of circular cylinders. *Mechanical Engineering Science Monograph*, **No. 4**.
- [27] Shellard, H. (1967). Collapse of cooling towers in a gale, ferrybridge, 1 november 1965. *Weather*, **22**(6), 232–240.
- [28] Soper, B. M. H. (1981). The effect of grid generated turbulence on the fluidelastic instability of tube bundle in cross flow. Dubrovnik, Paper No. P10.6.
- [29] Southworth, P. and Zdravkovich, M. (1975). Effect of grid-turbulence on the fluid-elastic vibrations of in-line tube banks in cross flow. *Journal of Sound and Vibration*, **39**(4), 461–469.
- [30] Spiteri, R. J. and Ruuth, S. J. (2002). A new class of optimal high-order strong-stability-preserving time discretization methods. *SIAM Journal on Numerical Analysis*, **40**(2), 469–491.
- [31] Vincent, A. and Meneguzzi, M. (1991). The satial structure and statistical properties of homogeneous turbulence. *Journal of Fluid Mechanics*, **225**, 1–20.